Energy Advances

ROYAL SOCIETY OF CHEMISTRY

PAPER

View Article Online
View Journal

Cite this: DOI: 10.1039/d6ya00011h

Cs_2CuLuY_6 (Y = Br, I) double halide perovskites: structural, optoelectronic, thermoelectric and thermo-mechanical insights for sustainable technologies

Md Shahazan Parves, *[ac] Rashel Mohammad Khokan,[bd] Md. Zahid Hasan [bc] and Hadjer Bendjilali *[ef]

This research provides an in-depth thorough assessment of the physical characteristics of Cs_2CuLuY_6 (Y = Br, I) materials using DFT. Structural stability is confirmed through tolerance factors, octahedral factors, and formation energy calculations, while elastic constants satisfy the Born stability criteria, indicating mechanical robustness. Phonon dispersion analysis reveals the absence of imaginary frequencies, confirming the dynamical stability of the investigated compounds. The evaluated Pugh's and Poisson's ratios suggest ductile behavior with noticeable elastic anisotropy. Electronic band structure analysis with GGA-PBE, TB-mBJ, and YS-PBE0 reveals that all investigated compounds are semiconductors with indirect band gaps. Optical analysis demonstrates strong absorption in the visible to UV region, highlighting their potential for optoelectronic and photovoltaic applications. Furthermore, thermoelectric analysis indicates promising thermoelectric performance with favorable figure-of-merit ($ZT \sim 1.0$) values over a wide temperature range, highlighting their potential for both low-temperature cooling and high-temperature heat recovery. These findings point to Cs_2CuLuY_6 alloy as a versatile potential material for renewable energy applications, predominantly in solar cell and thermoelectric applications.

Received 13th January 2026,
Accepted 28th March 2026

DOI: 10.1039/d6ya00011h

rsc.li/energy-advances

1. Introduction

The accelerated growth of the latest industrial systems and tech solutions requires the maturation of advanced materials with remarkable characteristics. In consideration of this, scientists have repeatedly studied novel classes of alloys to mitigate these issues. Included in these, double perovskite (DP) semiconductors have appeared as suitable choices due to their outstanding potential in next-generation optoelectronic and thermoelectric technology.[1] The potential of this class of compounds lies in their outstanding physical behavior, which is further enhanced by their structural adaptability. DP, in particular, exhibits versatile beneficial traits such as high carrier mobility, higher optical absorption, significant charge transport pathways, suitable band gap energies, lower effective masses, and noteworthy thermoelectric results.[2,3] The contribution of perovskite-based semiconductors covers far beyond electronics, shaping diverse aspects of daily life from healthcare, communication, and transportation to creative industries and more.[4] In contrast, those designed for thermoelectric materials must adequately harvest and transform remaining heat into functional power output. Of these, halide-based perovskite semiconductors have recently emerged as potential materials, demonstrating notable competence in utilization such as PSc and laser engineering.[5,6] Composites of organic and inorganic phase perovskites have attracted significant attention as a new generation of optoelectronic compounds, initially because of their unique solar energy transformation capabilities and their broadening role in devices such as LEDs and transistors.[7,8] Within the previous decade, integrated organic–inorganic hybrid perovskite frameworks have attracted attention as advanced optoelectronic materials due to their remarkable rise

[a] Graduate School of Environmental Engineering, The University of Kitakyushu, 1-1 Hibikino, Kitakyushu 808-0135, Japan. E-mail: Parveziiuc4708@gmail.com, g5maa402@eng.katakyu-u.ac.jp
[b] Materials Research and Simulation Lab, Department of Electrical and Electronic Engineering, International Islamic University Chittagong, Kumira, Chittagong 4318, Bangladesh
[c] Department of Electrical and Electronic Engineering, International Islamic University Chittagong, Kumira, Chittagong 4318, Bangladesh
[d] Faculty of Engineering, Kitami Institute of Technology, 165 Kouen-cho, Kitami, Hokkaido 090-8507, Japan
[e] Dielectric Materials and Polymers Team, Laboratory of Materials Physics, Faculty of Physics, University of Science and Technology Houari Boumediene USTHB, BP No 32, El Alia 16111, Algiers, Algeria. E-mail: hadjer.bendjilali@yahoo.com
[f] Condensed Matter and Sustainable Development Laboratory (LMCDD), University of Sidi Bel-Abbes, Sidi Bel-Abbes 22000, Algeria

in solar cell efficiencies, which have elevated from more or less 3.8% to 25.5%. This high performance, associated with their growing use in LEDs and transistor applications, highlights their versatility and technological utilization.[9–11] Nevertheless, halide perovskites containing lead pose significant health and environmental hazards, as their toxicity can result in severe detrimental effects on both human well-being and ecological systems.[12] To tackle these issues, DPs have drawn interest as a promising option in solar energy and optoelectronic applications, offering the advantage of adjusting a number of metal cations while ensuring high performance and eco-safety.[13] These materials are intended for use in photovoltaic devices, optoelectronic devices, and thermoelectric applications.[14,15] These compounds generally have the formula $A_2B'B''X_6$, where A indicates a monovalent cation, B′ and B″ are mono- and trivalent cations, respectively, and X indicates a halide anion. They offer the advantages of better stability and minimal toxicity while sustaining high performance. Cesium-based DPs, in particular, demonstrate considerable potential for detector technologies and scintillators owing to their wide band gaps, excellent radiation tolerance, and enhanced scintillation efficiency.[16,17] Investigation indicates that DPs containing K and Cs exhibit outstanding physical traits, placing them as strong contenders for radiation detection and photonic-crystal design, solar energy harvesting, energy storage applications, thermoelectric conversion, and photovoltaic devices.[18–21] Lead-free Cs-based inorganic DPs generally adopt the formula $Cs_2M^+M^{3+}X_6$, where M^+ is Ag^+, Ga^+, or Cu^+; M^{3+} is Bi^{3+} or In^{3+}; and X is Cl^-, Br^-, or I^-. Cs_2XBiBr_6 (X = Na, Ag, Cu and In) have been observed to achieve high solar energy conversion efficiencies.[22] Slavney *et al.*[23] studied the optoelectronic features of the $Cs_2AgBiBr_6$ DP and proposed further research on inorganic hybrid materials because of their strong prospects for photovoltaic and optoelectronic applications. Hamza Saci *et al.*[24] recently studied the structural and physical traits of the DPs Cs_2CuBiX_6 (X = F, Cl, Br, I), highlighting their suitability for solar energy and photovoltaic applications. Messaoud Caid *et al.*[25] investigated the physical properties of Cs_2CuIrF_6 materials using first-principles calculations using the GGA method, which resulted in an underestimated band gap, while suggesting that Cs_2CuIrF_6 is suitable for optoelectronic device applications. Studies have shown that In-based perovskites, including $X_2CuInCl_6$ and Rb_2InSbX_6 (X = Cl, Br), exhibit narrow band gaps, which contribute to notable thermoelectric performance and strong optical absorption properties.[26,27] Kamal *et al.*[28] also investigated the physical behavior of Rb_2AuBiX_6 (X = Br, Cl, F) and demonstrated that these compounds exhibit strong absorption and reflectivity within the visible light range. Furthermore, their strong Seebeck coefficients and significant thermoelectric figure of merit indicate their suitability for thermoelectric utilization. Abderrazak Boutramine *et al.*[29] investigated K_2InSbZ_6 (Z = I, Br, Cl, F) double perovskites using first-principles calculations and reported their structural stability, direct band gaps, and strong UV-visible optical activity with promising solar cell and thermoelectric performance. In another study, Adil Es-Smairi *et al.*[30] examined Na_2LiZF_6 (Z = Ir, Rh) double perovskites and confirmed their structural stability with wide indirect band gaps and strong UV optical absorption, indicating potential for UV optoelectronic devices. Furthermore, Messaoud Caid *et al.*[31–33] investigated several double perovskite compounds, including Pb_2FeSbO_6, Pb_2CoMoO_6, and Cs_2ABI_6 (AB = GeZn, SnBe), using first-principles DFT calculations. Their results showed that Pb_2FeSbO_6 behaves as a ferromagnetic semiconductor with promising thermoelectric performance, whereas Pb_2CoMoO_6 exhibits half-metallic ferromagnetic behavior suitable for spintronic applications. In addition, Cs_2GeZnI_6 and Cs_2SnBeI_6 were reported as stable halide double perovskites with indirect band gaps and favorable optical and thermoelectric properties for optoelectronic devices. Similarly, Samah Al-Qaisi *et al.*[34] studied K_2TlZI_6 (Z = Al, In) double perovskites using DFT and reported their structural stability, indirect band gaps, and promising optical and thermoelectric properties for energy applications. In another study, Aissa Benkatlane *et al.*[35] reported that Cs_2ABeCl_6 (A = Cd, Sn) double perovskites are stable semiconductors with strong UV absorption and promising thermoelectric properties. Another study by H. Rached *et al.*[36] explored Ba_2AlTMO_6 (TM = W, Re, Os) double perovskites and reported half-metallic ferromagnetic behavior with strong UV optical responses and promising thermoelectric performance. Hudabia Murtaza *et al.*[37–42] also investigated several double perovskite compounds belonging to the same family as the materials studied in this work using DFT, including Ba_2CdXO_6 (X = Mo, U), $Cs_2BB'H_6$ (B = Al, Na; B′ = Tl, In), $Cs_2BB'F_6$ (B = Rb, In, Na; B′ = Ir, As, Rh), K_2CuBiX_6 (X = I, Br, Cl), $K_2NaGaBr_6$, $K_2RbTlBr_6$ and $Cs_2LiTlCl_6$. Their studies reported thermodynamic stability and semiconducting band gaps, while several compounds exhibited strong optical absorption in the visible-UV region and promising thermoelectric performance with appreciable *ZT* values, highlighting their potential for optoelectronic and renewable energy applications. SMH Qaid *et al.*[43,44] also investigated Rb_2ASbX_6 (A = Tl, Cu; X = I, Cl) double perovskites and Rb_2XRhF_6 (X = Li, Ag) halide perovskites using DFT. Their studies reported structural stability, suitable semiconducting band gaps, strong optical absorption in the visible-UV region, and promising thermoelectric performance for energy-related applications. Junaid Munir *et al.*[45] reported with DFT calculations that K_2TlAsX_6 (X = Cl, Br) double perovskites are structurally stable with direct band gaps and promising optical and transport properties for optoelectronic and energy applications. Although numerous recent studies have focused on halide-based DPs, the rising demand for high-potential optoelectronic compounds underscores the importance of discovering and evaluating novel candidates within the DP family. Moreover, in this article, we conducted a pioneering investigation on the Cs_2CuLuY_6 DP compounds using the DFT method, including GGA-PBE, TB-mBJ, and YS-PBE0 functionals. These materials were chosen because Cs-based double perovskites with the general formula $A_2B'B''X_6$ represent promising lead-free and environmentally friendly alternatives to Pb-based perovskites widely used in optoelectronic/thermoelectric devices. Furthermore, halide substitution (Br *vs.* I) provides an effective strategy

for tuning the electronic structure, as replacing Br with the heavier I atom generally leads to a reduction in the band gap and modifies the optical response. This work aims to provide an in-depth investigation of the fundamental physical properties of Cs_2CuLuY_6. Utilizing this methodology, our goal is to conduct an in-depth theoretical calculation of these compounds and highlight their potential for real-world manufacturing applications. This study looks for crucial insights that can guide reliable predictions of their behavior across various technological implementations.

2. Computational techniques

We used the WIEN2k code by DFT to calculate the numerous features of the Cs_2CuLuY_6 materials, which are impacted by the FP-LAPW method.[46] The structural relaxation was carried out using the generalised gradient approximation (GGA), with the Perdew–Burke–Ernzerhof (PBE) functional employed to model exchange–correlation effects precisely.[47] The exchange–correlation energy in GGA is expressed as:

$$E_{XC}^{GGA} = \int \rho(r)\varepsilon_x^{hom}(\rho(r))F_{Xc}\rho(r), \nabla\rho(r))dr \qquad (1)$$

where ρ is the electron density and $\nabla\rho$ is the gradient, F_{Xc} is the dimensionless factor, and ε_x^{hom} is the exchange energy of the homogeneous system. Convergence was checked to verify that the total energy is minimum in relation to the size of the basis set ($R \times K_{max} = 8$) and the k-point ($13 \times 13 \times 13$). The total energy convergence criterion is set to 10^{-6} Ry as the standard threshold. The optoelectronic features are measured utilizing a combination of approaches, including the GGA-PBE, the TB-mBJ potential and the hybrid YS-PBE0 functional, to accurately characterize the electronic and optical properties.[48] The TB-mBJ exchange potential is expressed as:

$$V_x^{TB\text{-}mBJ(r)} = cV_x^{BR}(r) + (3c-2)\frac{1}{\pi}\sqrt{\frac{5}{12}}\sqrt{\frac{2t(r)}{\rho(r)}} \qquad (2)$$

where V_x^{BR} is the Becke–Roussel potential, $t(r)$ is the kinetic energy density, and $\rho(r)$ is the electron density. The thermoelectric performance was evaluated employing the BoltzTraP2 code, which employs electronic structure information obtained from WIEN2k to solve the semiclassical Boltzmann transport equations.[49] The semi-classical transport coefficients are evaluated utilizing relaxation time approximation (RTA = 10^{-14} s). Phonon dispersion calculations were carried out using the linear response method within the framework of density functional perturbation theory (DFPT), as implemented in the CASTEP code. Norm-conserving pseudopotentials were employed to accurately describe the electron–ion interactions.

3. Results and discussion

3.1. Structural properties and dynamical stability

In DP structures, distinct cations are placed in the A and B sites, giving rise to a unique ordered arrangement in the lattice framework.[50] DPs are typically divided into two types: $A'A''B_2X_6$ (A-site DPs) and $A_2B'B''X_6$ (B-site DPs). In these lattices, the larger A-type cations occupy the A-sites, while the smaller B and B′ cations are positioned at the B and B′ sites, respectively. The X-sites are typically filled by halide anions. All the Cs_2CuLuY_6 (Y = Br, I) adopt the B-site double perovskite configuration. These materials crystallise in a cubic lattice and are classified under the $Fm\bar{3}m$ space group. The cubic crystal structure of the Cs_2CuLuY_6 (Y = Br, I) double perovskite is shown in Fig. 1. The Cs_2CuLuY_6 (Y = Br, I) possess a unit cell containing 40 atoms, corresponding to four formula units with a stoichiometric ratio of 2 : 1 : 1 : 6. The Wyckoff positions are assigned as follows: Cs occupies 8c (0.25, 0.25, 0.25), Cu resides at 4a (0.5, 0.5, 0.5), Lu is located at 4b (0, 0, 0), and Br/I atoms are positioned at 24e (0.25, 0, 0).

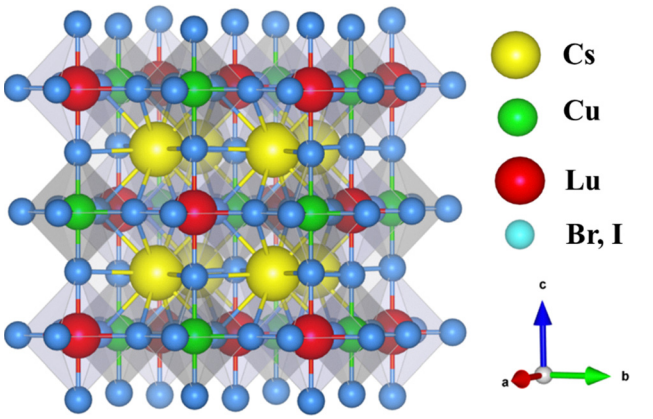

Fig. 1 Crystal structures of Cs_2CuLuY_6 (Y = Br, I).

The crystal geometry of Cs_2CuLuY_6 (Y = Br, I) was optimized using the GGA-PBE exchange-correlation functional. The lattice constant was determined by locating the equilibrium volume (V) corresponding to the minimum total energy (E_0).

The structural stability of a double perovskite can be assessed through the tolerance factor (τ_1), the newly proposed physically based tolerance factor (τ_2), and the octahedral factor (μ). These stability metrics were evaluated using the relationships presented in the following equations:[51,52]

$$\tau_1 = \frac{R_{Cs} + R_Y}{\sqrt{2}\left(\frac{R_{Cu} + R_{Lu}}{2} R_Y\right)} \qquad (3)$$

$$\tau_2 = \frac{R_Y}{R_{Cu}} n_{Cs}\left(n_{Cs} - \frac{\frac{R_{Cs}}{R_{Cu}}}{\ln\frac{R_{Cs}}{R_{Cu}}}\right) \qquad (4)$$

$$\mu = \frac{R_{Cu} + R_{Lu}}{2R_Y} \qquad (5)$$

In the case of eqn (3)–(5), R_{Cs}, R_{Cu}, R_{Lu}, and R_Y (Br, I) denote the ionic radii of Cs, Lu, and Br/I, respectively, and n_{Cs} is the oxidation state of the Cs site. A compound is considered to be cubically stable if the tolerance factor (τ_1) lies within the range

Table 1 Structural characteristics of the investigated compounds with reference materials

Materials	Lattice constant, $a = b = c$ (Å)	Minimum volume, V (Bohr^3)	Minimum energy, E_0 (Ry)	Tolerance factor (τ_1)	Physically based tolerance factor (τ_2)	Octahedral factor (μ)	Formation energy, E_f (eV per atom)	Ref.
Cs_2CuLuI_6	11.84	2805.13	−49 063.02	0.956	4.957	0.370	−1.615	This study
$Cs_2CuLuBr_6$	10.99	2239.48	−94 914.06	0.978	4.416	0.416	−2.172	This study
K_2InSbI_6	12.47	3273.54	−112 571.67	0.911	—	0.354	−1.868	29
$K_2InSbBr_6$	11.73	2724.99	−58 422.88	0.929	—	0.398	−2.107	
$K_2InSbCl_6$	11.25	2399.75	−32 681.32	0.942	—	0.431	−2.368	
K_2InSbF_6	09.61	1497.58	−28 341.59	0.995	—	0.586	−2.989	
Cs_2GeZnI_6	11.83	—	—	0.983	4.178	0.391	−2.264	33
Cs_2SnBeI_6	11.975	—	—	0.962	4.050	0.426	−2.618	
K_2TlAlI_6	12.21	—	—	0.99	—	—	−1.95	34
$Cs_2CdBeCl_6$	10.27	—	—	1.039	—	0.440	−2.644	35
$Cs_2SnBeCl_6$	10.60	—	—	0.950	—	0.380	−2.904	

of 0.813 to 1.107, while the octahedral factor ranges from 0.41 to 0.89.[53] Furthermore, our study's computed new tolerance factor is more precise than other techniques for predicting structural stability. It is expected that for cubically stable perovskites, τ_2 will be smaller than 4.18.[54] According to the data listed in Table 1, it is obvious that all the studied compounds are cubically stable.

Furthermore, the formation energy offers another technique to determine the stability of the double halide perovskites, Cs_2CuLuY_6 (Y = Br, I), which can be estimated using the given formula:[55]

$$E_f = \frac{E_{Cs_2CuIrY_6} - n_{Cs} \times \frac{E_{Cs}}{k} - n_{Cu} \times \frac{E_{Cu}}{l} - n_{Lu} \times \frac{E_{Lu}}{m} - n_Y \times \frac{E_Y}{p}}{N} \quad (6)$$

where $E_{Cs_2CuLuY_6}$ represents the total energy of Cs_2CuLuY_6 and E_{Cs}, E_{Cu}, E_{Lu}, and E_Y represent the energy of Cs, Cu, Lu, and Y, respectively. The n denotes the count of Cs, Cu, Lu, and Y atoms, and the individual free state energy of the total atoms, respectively. The constants k, l, m, and p are individual atoms per unit cell. N represents the total number of atoms. Negative values of formation energy indicate the stability of compounds.

The formation energy (E_f) serves as an important measure of thermodynamic stability, where a more negative value indicates a higher degree of stability. As presented in Table 1, all the investigated compounds possess negative formation energies, confirming their thermodynamic stability. Table 1 indicates that the calculated properties of our studied material are very close to those reported for other Cs-based and similar series double perovskite (DP) reference materials, which supports the reliability and validity of the present study. We have also presented the variation of energy with respect to volume for both compounds under investigation in Fig. 2.

The phonon dispersion relationships of $Cs_2CuLuBr_6$ and Cs_2CuLuI_6 were calculated to evaluate their dynamical stability, and the results are presented in Fig. 3. As can be seen, no imaginary (negative) phonon frequencies appear throughout the entire Brillouin zone for either compound, confirming their dynamical stability. Each primitive unit cell contains ten atoms, giving rise to a total of thirty phonon branches, including three acoustic and twenty-seven optical modes. The acoustic branches originate from the Γ point and increase smoothly along the high-symmetry directions, while the remaining branches correspond to optical modes distributed in the higher-frequency region. A noticeable separation between

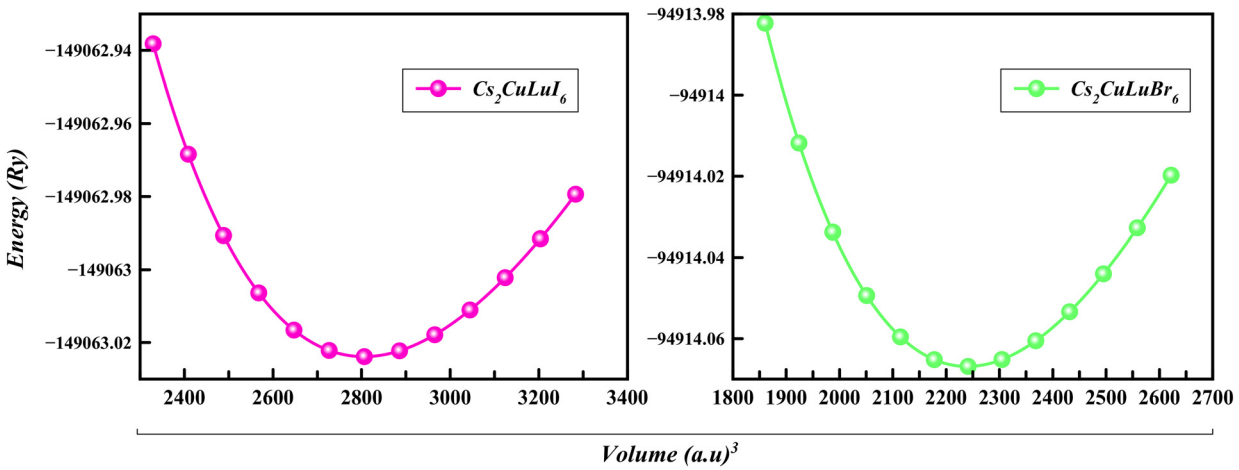

Fig. 2 Minimum energy (E) *vs.* volume (V) optimization curve.

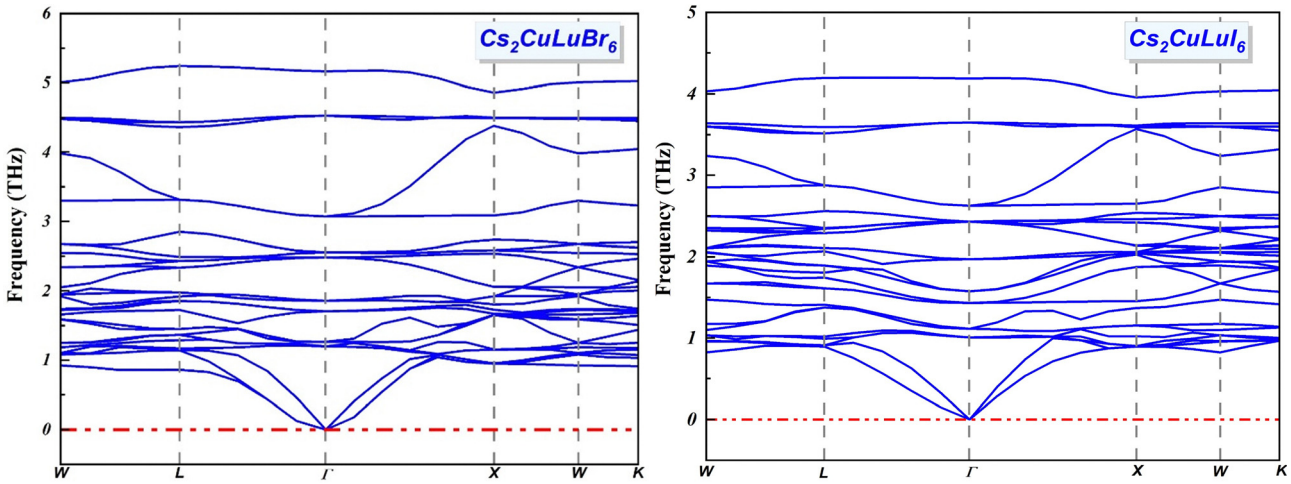

Fig. 3 Phonon dispersion curves for the double perovskites $Cs_2CuLuBr_6$ and Cs_2CuLuI_6.

certain optical branches, as well as between the acoustic and low-frequency optical branches, can also be observed, indicating the presence of phonon band gaps. Furthermore, both compounds exhibit very similar phonon dispersion characteristics; however, $Cs_2CuLuBr_6$ shows slightly higher phonon frequencies compared with Cs_2CuLuI_6, which can be attributed to the relatively lighter atomic mass of Br compared with I, shifting the modes to higher frequencies.

3.2. Electronic characteristics, charge carrier effective masses, and density of states analysis

Evaluating the electronic characteristics of a material is essential for determining its optoelectronic and photovoltaic performance. Key factors include the band gap, which governs light absorption capability, and the density of states, describing the distribution of electronic states both in total and for individual elements. Fig. 4 displays the band structure diagrams of the Cs_2CuLuY_6 (Y = Br, I). In these figures, the vertical axis indicates the energy levels, whereas the horizontal axis denotes the wave vector (k), mapped across various high-symmetry directions within the bulk Brillouin zone. The BS is plotted along the high-symmetry W–L–Γ–X–W–K path. The Fermi level, indicated by a red dashed line at zero energy level, separates the VB and CB. In contrast, the band gap was evaluated using the TB-mBJ and YS-PBE0 exchange correlation potentials, since these methods provide a more accurate description of the electronic structure and produce values that better correspond to experimental observations.[56] Table 2 presents the band gap values of our investigated Cs_2CuLuY_6 compounds, calculated using three different methods. The evaluated band gap values with GGA-PBE, TB-mBJ, and YS-PBE0 reflect the smallest energy separation between the VB generally occupied by e^- and the CB, where e^- can freely move and participate in electrical conductivity. Here, the valence band maximum (VBM) and conduction band minimum (CBM) occur at different symmetry points, move from L to the Γ point, which ensures that the material shows an indirect band gap. Similar indirect band gap behavior has also been reported in related double perovskite systems such as $Rb_2TlB'I_6$ (B′ = As, Ga), Rb_2TlInX_6 (X = Cl, I) and Cs_2AgBiI_6 through previous DFT investigations.[57–59] The computed band gaps for the studied compounds are as follows: $Cs_2CuLuBr_6$ yields 1.67 eV (GGA-PBE), 2.52 eV (TB-mBJ), and 2.76 eV (YS-PBE0); while Cs_2CuLuI_6 provides 1.24 eV (GGA-PBE), 1.99 eV (TB-mBJ), and 2.09 eV (YS-PBE0). These values indicate that Cs_2CuLuY_6 exhibits a semiconductor nature. Since semiconductors with band gaps of 1.62 to 3.10 eV are good at absorbing visible light effectively, Cs_2CuLuY_6 compounds exhibit an energy range window for use in light-harvesting and optoelectronic applications.[60] In addition, traditional perovskite materials generally possess band gaps in the range of 0.8 to 2.2 eV, making them highly favorable for use in solar energy conversion technologies.[61,62] The indirect band gap characteristic implies that electron–hole recombination requires phonon assistance, leading to lower radiative recombination rates compared with direct band gap semiconductors. However, this feature often results in longer carrier lifetimes and reduced recombination losses, which can enhance charge transport and carrier collection efficiency. Consequently, although indirect band gap materials are less suitable for light-emitting devices, they remain promising for applications such as photovoltaic absorbers, photodetectors, and thermoelectric systems. Additionally, the valence band states near the Fermi level show greater activity than those of the conduction band (CB), suggesting that these compounds are particularly favorable for technologies involving valence band (VB) related electronic transitions.[63,64]

3.2.1 The effective mass of the charge carrier. The effective mass does not represent the actual physical mass of electrons or holes but reflects how easily they can move through a compound. As it strongly affects charge carrier mobility, electrical resistance, and optical absorption, its assessment is crucial. In this study, a specific mathematical equation has been used to calculate the effective masses for Cs_2CuLuY_6 compounds:[65]

$$\frac{1}{m^*} = \frac{1}{\hbar^2}\frac{\partial^2 E_n\left(\vec{k}\right)}{\partial k^2} \quad (7)$$

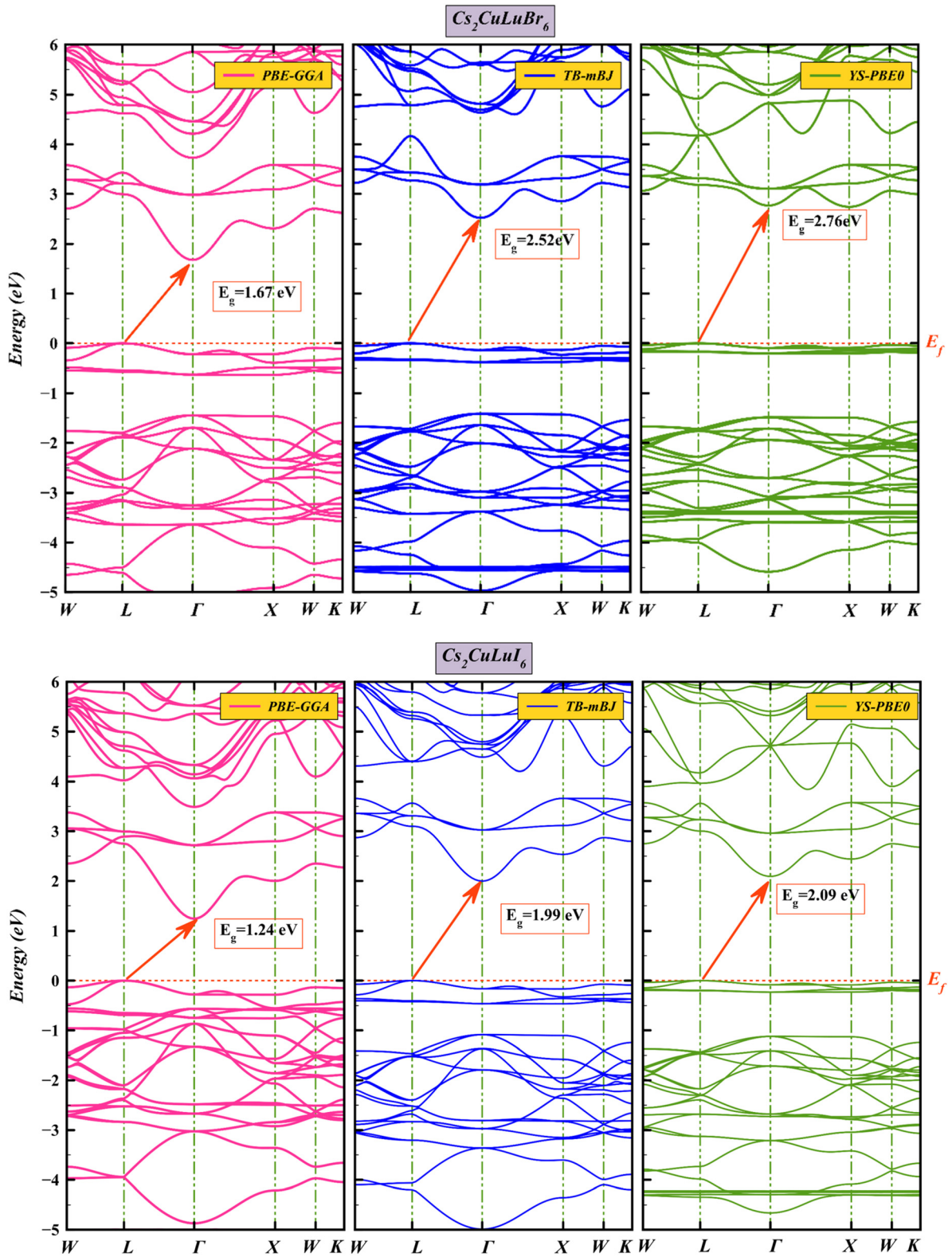

Fig. 4 Band diagram of (a) $Cs_2CuLuBr_6$ and (b) Cs_2CuLuI_6.

Here, the reduced Planck constant ($\hbar$), the material's energy bands $E(k)$, and the wave vector k, which defines the orientation of carrier motion, are included. The calculations of effective mass provide insights into the mobility of electrons and holes

Table 2 Computed band gaps for investigated compounds with reference materials

Compound	GGA-PBE (eV)	TB-BJ (eV)	YS-PBE0 (eV)	Nature	Ref.
Cs_2CuLuI_6	1.24	1.99	2.09	Indirect	This work
$Cs_2CuLuBr_6$	1.67	2.52	2.76		This work
Cs_2GeZnI_6	0.52	1.12	—		33
Cs_2SnBeI_6	1.05	1.55	—		
$Cs_2SnBeCl_6$	2.58	—	—		35
$Cs_2CdBeCl_6$	1.98	—	—	Direct	
K_2TlAlI_6	1.56	2.25	—	Indirect	34
K_2TllnI_6	0.82	1.37	—		

Table 3 Estimated effective masses of holes m_h^* and electrons m_e^*

Compound	Approach	m_h^*/m_0	m_e^*/m_0
Cs_2CuLuI_6	TB-mBJ	1.21	0.28
$Cs_2CuLuBr_6$		1.23	0.33

within the compounds, strongly impacting the effectiveness of photovoltaic applications. The findings effective masses are present in Table 3. In general, holes show higher effective masses than electrons because the valence band, where holes reside, has a flatter curvature compared to the sharply curved conduction band that hosts electrons. This gentler curvature results in a higher effective mass, meaning the holes move more slowly through the lattice.

For the Cs_2CuLuY_6, a consistent trend is noticed: the effective masses of holes exceed those of electrons, revealing that the VBM is less curved than the CBM. Investigation of both the band gap and effective masses underscores the suitability of our investigated materials for a range of optoelectronic technologies. The evaluated effective masses for holes (m_h^*) and electrons (m_e^*) are: 1.21 and 0.28 for Cs_2CuLuI_6, and 1.23 and 0.33 for $Cs_2CuLuBr_6$. The relatively low electron effective masses encourage elevated carrier mobility, which is strongly beneficial for energy-related applications such as infrared sensors, detectors, solar cells, and other optoelectronic devices. Cs_2CuLuY_6 stands out as the most promising candidate for photovoltaic and efficient solar energy applications due to its optimal combination of band gap and charge transport features.

3.2.2 Density of states. The total density of states (TDOS) at a specified energy assesses the number of electronic states (ES) accessible at every energy level, offering a complete picture of the compound's energy level scheme. Additionally, it elucidates the correlation between energy level and the CB and VB and also quantifies the atomic contribution. As visualized in Fig. 5, the TDOS of Cs_2CuLuY_6 (Y = Br, I) DP elucidates phenomenal compatibility with their band gap values. In Fig. 5, the red line at 0 eV implies the location of the Fermi level. In Cs_2CuLuY_6, the Fermi level is predominantly governed by the d orbitals of Cu. Investigation of the same data reflects that the VB is primarily derived from Cu d and Br/I p orbitals, while participation from Cs s and Lu d orbitals is marginal. In contrast, the CB of Cs_2CuLuY_6 (Y = Br, I) is predominantly governed by the d orbitals of Lu, with minor contributions associated with the p orbitals of Br or I.

3.2.3 Charge density mapping. Charge density mapping (CDM) functions as a reliable tool to demonstrate the positional allocation of electrons within the bulk of the compounds. This approach provides key insights into the chemical bonding, electronic structure, and intrinsic characteristics of a compound. For Cs_2CuLuY_6, CDM enables a comprehensive analysis of interatomic bonding. These representations emphasize the crystal lattice's zones of high and low density of electrons, enabling it to be feasible to identify whether a bond is mostly metallic, covalent, or ionic.

Cs–Y (Cs–Br, and Cs–I) interactions. Generally, halogen atoms establish ionic bonds with Cs; Br and I atoms possess a high electron density due to their superior electronegativity; Cs^+ ions, on the other hand, prefer chiefly ionic bonding with the

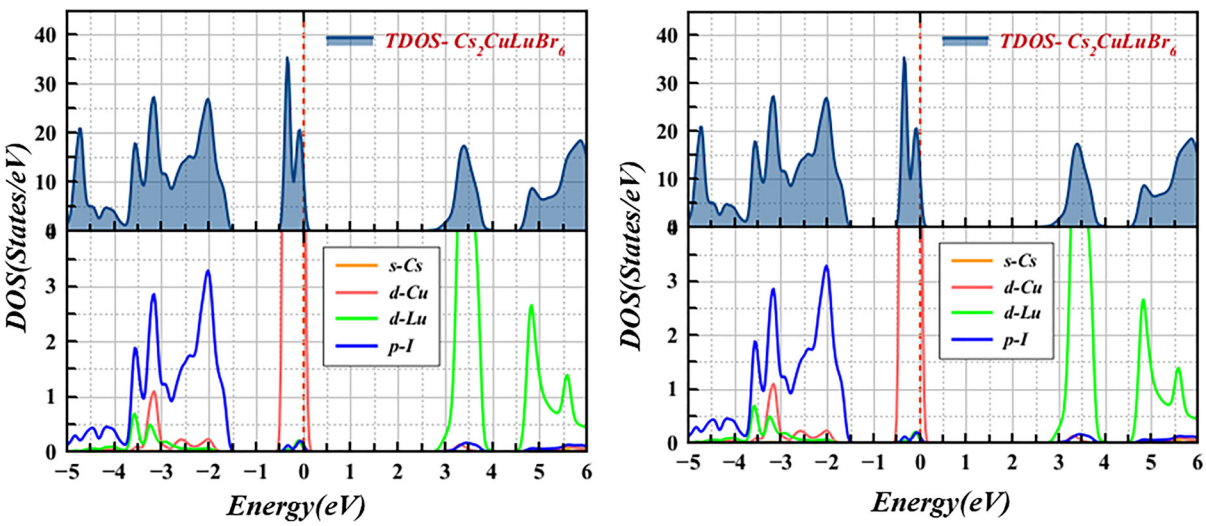

Fig. 5 Full DOS and partial DOS of Cs_2CuLuY_6 (Y = Br, I).

halide anions (Br^-/I^-) owing to their high ionic radius and fairly low charge density.

Cu–Y (Cu–Br/I) interactions. The octahedral frame's center transition metal (Cu) has enormous interaction with the neighbouring F molecules. Cu, which can exist as Cu^+ and Cu^{2+}, forms bonds with a crucial covalent characteristic because of its comparatively higher electronegativity than Cs.

Lu–Br/I interactions. Despite Lu's elevated oxidation state and tendency to employ d-orbitals in bonding with Br/I, the Lu–Br/I interactions reveal a robust covalent nature with an aberrant ionic part. Similar outcomes have already been reported in previous studies.[66,67]

Cu–Lu (Cu–Lu) interactions. Depending on the specific metal involved, the electron density near Cu and Lu atoms fluctuates, suggesting that the percentage of covalent and ionic nature in the bonds varies.

In summary, the particular transition metal Cu affects the bonding behavior, which shows a combination of covalent and ionic interactions in Cs_2CuLuY_6 (Fig. 6).

3.3. Optical properties

The way a material reacts with incoming light determines its optical traits, which are vital for evaluating the gadget's functionality. The dielectric constant $\varepsilon(\omega)$ plays an important role in optoelectronic and photovoltaic applications. A low dielectric constant accelerates charge carrier recombination, whereas a high dielectric constant enables efficient charge storage and improved device performance.[68] Therefore, evaluating the dielectric constant is essential for determining the suitability of semiconductor materials for practical applications. The complex dielectric function, which can be represented employing the Ehrenreich and Cohen formalism, is frequently used to quantify this light-matter[69] as $\varepsilon(\omega) = \varepsilon_1(\omega) + i\varepsilon_2(\omega)$. Here, ω denotes the angular frequency, whereas $\varepsilon_1(\omega)$ and $\varepsilon_2(\omega)$ stand for the real and imaginary parts, respectively. The degree of polarization the compound may get in the presence of an external electric field is shown by the real components evaluated utilizing the Kramers–Kronig equation. Conversely, the imaginary part, evaluated from the Kohn–Sham formalism,[11] characterizes the compound's light absorption capability.

$$\varepsilon_1(\omega) = 1 + \frac{2}{\pi} p \int_0 \frac{\alpha_{\omega' * \varepsilon_2(\omega')}}{\omega'^2 - \omega^2} d\omega \quad (8)$$

$$\varepsilon_2(\omega) = \frac{2\pi e^2}{\Omega \varepsilon_0} \sum_{k,\nu,c} \left| \Psi_k^c | \hat{u} \cdot \vec{r} | \Psi_k^\nu \right|^2 \delta\left(E_k^c - E_k^\nu - E\right) \quad (9)$$

where p designates the principal parameter. Meanwhile, the second relationship employs symbols like v, e, h, p, k_n, and k'_n, which denote the unit cell volume, electronic charge, reduced Planck's constant, momentum transition operator, valence band state, and conduction band state, respectively. The measured static dielectric constant $\varepsilon_1(0)$ was determined to be around 2.90 for $Cs_2CuLuBr_6$ and 3.72 for Cs_2CuLuI_6. These data are depicted in Fig. 7(a). Usually, materials with higher static dielectric constants generally inhibit charge carrier recombination significantly, consequently boosting the performance of optoelectronic apparatus. This suggests that $Cs_2CuLuBr_6$ is expected to demonstrate greater optoelectronic attributes than Cs_2CuLuI_6, owing to their larger $\varepsilon_1(0)$ values. Additionally, the evaluated static dielectric constant values for the Cs_2CuLuY_6 compounds lie in the range of 2.0 to 10.0, proposing their feasibility for a wide range of technological applications, such as capacitor technologies and optoelectronic devices.[70] Notably, a higher $\varepsilon_1(0)$ value signifies strengthened reactivity to impinging electromagnetic radiation. The researched compounds show marked optical functionality across each of the VR and UV zones, as revealed by the peak data of $\varepsilon_1(\omega)$.

This correlates with Penn's model, verifying an inverse association with the static dielectric constant and the band gap.[71]

$$\varepsilon_1(0) \approx 1 + \left[\frac{\hbar\omega_p}{E_g}\right]^2 \quad (10)$$

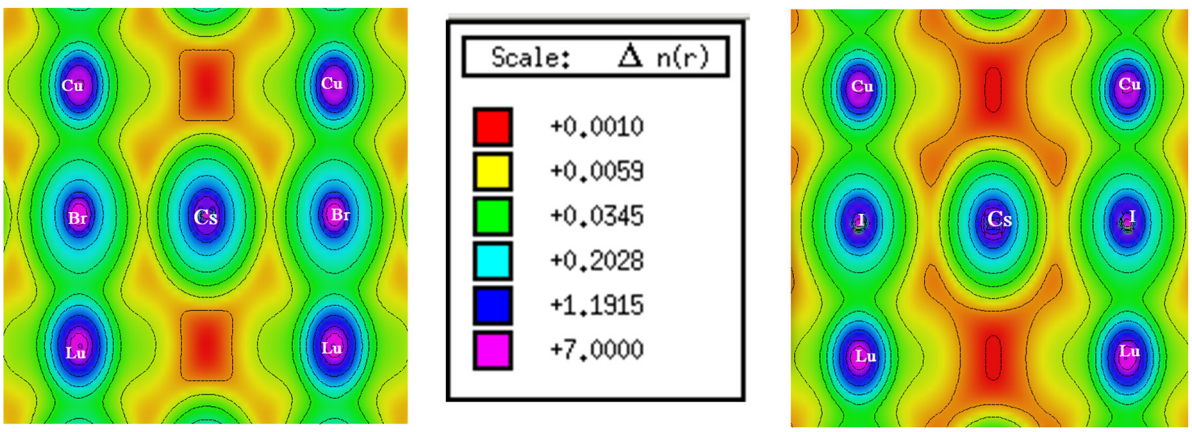

Fig. 6 Charge density mapping of Cs_2CuLuY_6 (Y = Br, I).

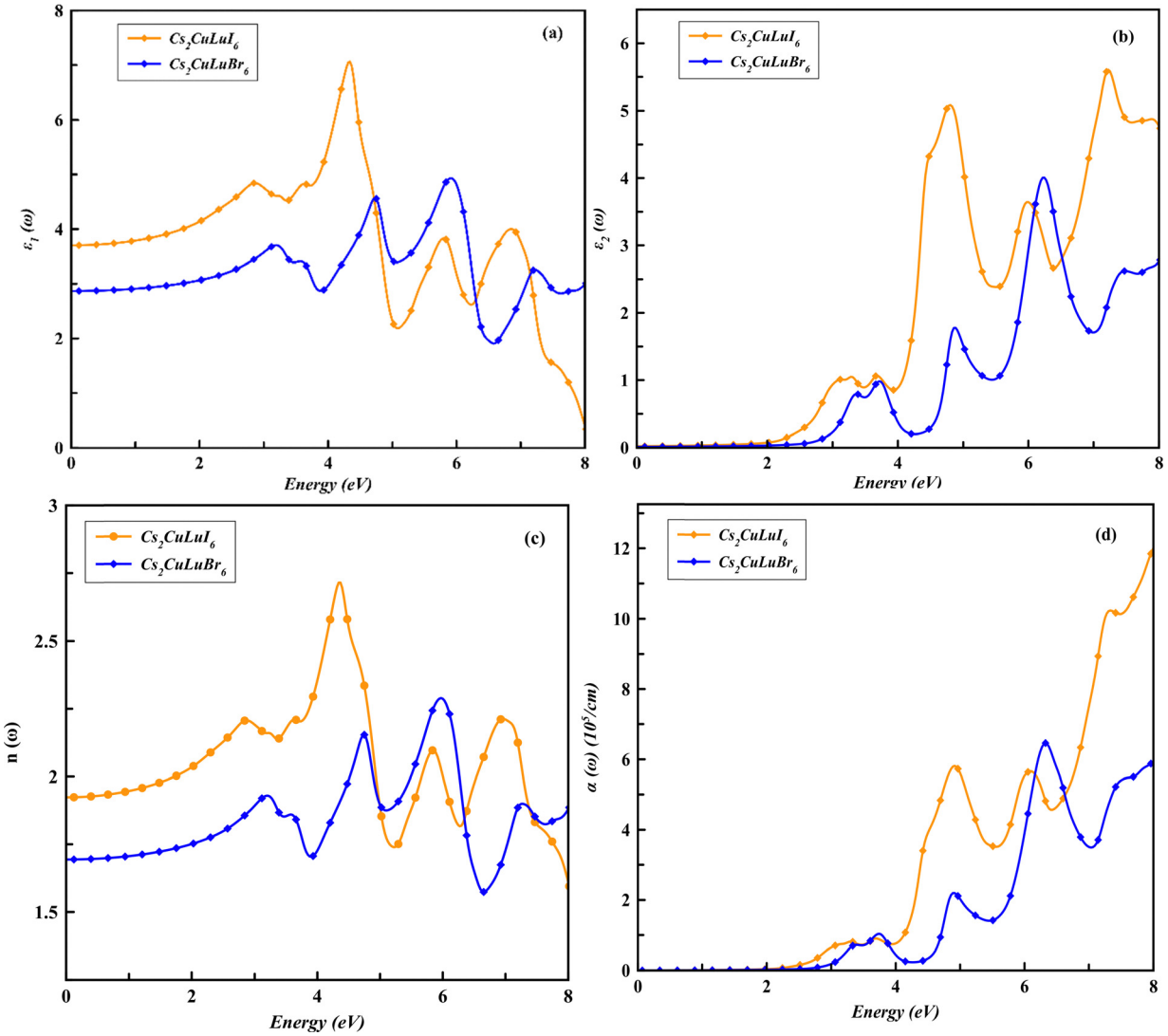

Fig. 7 (a) $\varepsilon_1(\omega)$: the real part of the dielectric constant, (b) $\varepsilon_2(\omega)$: imaginary part of the dielectric constant, (c) $n(\omega)$: refractive index and (d) $\alpha(\omega)$: absorption coefficient for the studied compounds.

Here, $\hbar$ is the reduced Planck constant and ω_p denotes the plasma frequency. The highest values of the real dielectric constant in the UV zone were identified to be 5.1 for $Cs_2CuLuBr_6$ and 7.0 for Cs_2CuLuI_6. $\varepsilon_1(0)$ is strongly correlated to a compound's polarizability, signifying that greater polarizability results in optimal reaction to an applied electric field of materials, resulting in an elevated dielectric constant. Hence, Cs_2CuLuI_6 outperform polarizability in the UV zone, with the highest peak at 4.0 eV. When photon energy rises, the peak values of their polarization curves gradually decrease, suggesting that the material's responsiveness to an external electric field diminishes when moving from lower to higher energy ranges.

$\varepsilon_2(\omega)$ represents the material's capability to absorb electromagnetic radiation. Fig. 7(b) shows the first absorption peaks (FAP) lie around 3.1 eV for each Cs_2CuLuI_6 and $Cs_2CuLuBr_6$, indicating strong absorption within the visible range. These absorption energies, spanning the VR to UV zone, indicate the studied compounds are efficient alloys for making optoelectronic systems operating across this spectral zone.

Derived from $\varepsilon_1(\omega)$ and $\varepsilon_2(\omega)$, various optical parameters were calculated, like the real component of optical conductivity, the complex refractive index, the absorption coefficient, reflectivity, and the electron energy loss spectrum. All these optical parameters were evaluated utilizing below standard formulas are widely accepted.[72]

$$n(\omega) = \frac{1}{\sqrt{2}}\left\{\sqrt{\varepsilon_1^2(\omega) + \varepsilon_2^2(\omega)} + \varepsilon_1(\omega)\right\}^{\frac{1}{2}} \quad (11)$$

$$k(\omega) = \frac{1}{\sqrt{2}}\left\{\sqrt{\varepsilon_1^2(\omega) + \varepsilon_2^2(\omega)} - \varepsilon_1(\omega)\right\}^{\frac{1}{2}} \quad (12)$$

$$I(\omega) = \sqrt{2}\omega\left\{\sqrt{\varepsilon_1^2(\omega) + \varepsilon_2^2(\omega)} + \varepsilon_1(\omega)\right\}^{\frac{1}{2}} \quad (13)$$

$$R(\omega) = \frac{\{n(\omega) - 1\}^2 + k^2(\omega)}{\{n(\omega) + 1\}^2 + k^2(\omega)} \quad (14)$$

The refractive index $n(\omega)$ plays a vital role in designing optical instruments. It is commonly used to assess the functionality of materials in utilization such as solar cells and sensors. The real part of the refractive index, $n(\omega)$, indicates how much light is bent or refracted when passing through a material, thereby reflecting its optical transparency. The energy-dependent variation of $n(\omega)$ is illustrated in Fig. 7(c). Notably, the trends observed in $n(\omega)$ closely follow those of the dielectric function $\varepsilon(\omega)$, in accordance with the established theoretical relationship.[73]

$$n^2(0) = \varepsilon_1(0) \quad (15)$$

The refractive index $n(\omega)$ exhibited static values of 2.00 and 1.92 at the first absorption peak for Cs_2CuLuI_6 and $Cs_2CuLuBr_6$ displayed values of 1.72. The maximum refractive index was observed at 2.71 at 4.31 eV and 2.32 at 6.00 eV for Cs_2CuLuI_6 and $Cs_2CuLuBr_6$, as illustrated in Fig. 7(c). These results indicate significant optical responsiveness within the UV to visible energy range for all investigated compounds. Compared to silicon nitride (refractive index of 1.9),[74] such materials are more ideal for solar energy devices. Besides, the enhanced transmittance is demonstrated by the antireflective.

The absorption coefficient, $\alpha(\omega)$, is a metric for assessing the performance of photoelectric gadgets, as it regulates the generation of charge carriers. If it has a high value, it signifies an improved absorptivity, thereby enhancement in the photoresponse in systems like solar cells. The material's optical response within the VR zone of 1.6 to 3.2 eV, corresponding to wavelengths at 780 to 380 nm, is vital for applications in solar energy technologies and photonic gadgets. The first prominent peaks of the absorption coefficient ($\alpha_{max}(\omega)$) in the VR to UV region are found at 3.1 eV with 0.42×10^5 cm^{-1} for Cs_2CuLuI_6, and 3.8 eV with 0.48×10^5 cm^{-1} for $Cs_2CuLuBr_6$, as shown in Fig. 7(d). These results are well matched with the absorption coefficient observed in renowned solar cell materials, such as Si, revealing $\alpha(\omega)$ between 10^3 and 10^5 cm^{-1}, CIGS with values between 10^4 and 10^5 cm^{-1}, and CdTe demonstrating similar levels of 10^4 to 10^5 cm^{-1}.[75] Both investigated materials revealed steadily enhancing absorption coefficients across the near VR, with pronounced absorption extending well into the UV region. Each of the researched materials demonstrates strong absorptivity within the visible range, indicating their appropriateness as absorber layers in photovoltaic applications. This trait boosts their ability to capture incident light, indicating their potential to improve solar cell performance and overall energy conversion efficiency.[76] Moreover, our researched alloys exhibit greater absorption coefficients than other DPs (in the order of 10^4), such as Cs_2AgBiI_6,[77] Cs_2InCoX_6[78] and Cs_2CuBiX_6 (X = Cl/Br/I).[79]

The optical conductivity of a compound is intensely determined by its photon absorptivity. It serves as a metric that links optical reflectivity with frequency and indicates how efficiently carrier mobility enables photoconductivity. The peak optical conductivity of Cs_2CuLuI_6 is above 4 eV, and for $Cs_2CuLuBr_6$ at 6.9 to 7.8 eV, with associated conductivity values of 5500 and 3400 Ω^{-1} cm^{-1}, respectively, as shown in Fig. 8(a). All materials demonstrate fairly low optical conductivity throughout the visible spectrum, which increases gradually with increasing photon energy. A wider absorption band that spreads toward a larger photon energy above the initial peak implies deeper electronic transitions within the compounds. Such spectral characteristics offer valuable information about the underlying electronic structure and highlight the potential of Cs_2CuLuY_6 materials for wide-ranging optoelectronic gadgets.

The percentage of falling light in the surface of materials that is reflected off a semiconductor's surface is measured by optical reflectivity $R(\omega)$. The initial reflectivity values were computed as 0.10 and 0.07 for Cs_2CuLuI_6 and $Cs_2CuLuBr_6$, respectively. The values of $R(\omega)$ are elevated with rising photon energy, resulting in pronounced peaks in the visible range for both compounds. The peak reflectivity in the UV zone was found to be 0.28 and 0.20 for Cs_2CuLuI_6 and $Cs_2CuLuBr_6$, respectively, as illustrated in Fig. 8(b). Reflectivity increases with photon energy and becomes higher in the ultraviolet (UV) region, showing a trend similar to other double perovskites.[80] Additionally, the coupling of high-index with low reflectance makes the Cs_2CuLuY_6 material promising for applications in LEDs and other optoelectronic systems.[81] For both compounds, reflectance remains low within the energy range extending below the bandgap. This suggests that Cs_2CuLuY_6 are transparent to incident photons within this range, making them highly suitable candidates for lenses designed to operate in this range.[82]

DP materials' energy loss spectra indicate their ability to scatter light at different photon energies or frequencies. As depicted in Fig. 8(c), the Cs_2CuLuY_6 materials reveal their most pronounced loss function peaks in the UV region, achieving values of 0.21 and 0.25 for Cs_2CuLuI_6 and $Cs_2CuLuBr_6$ at photon energies of 5.2 and 6.7 eV, respectively. In the visible spectrum, these materials show low energy-loss values. With increasing photon energy, the loss spectra follow a fluctuating pattern of rise and fall, highlighting the dynamic response of these DPs to incident radiation.

3.4. Thermoelectric (TE) properties

As global energy needs continue to rise, researchers are increasingly exploring advanced approaches to capture renewable and environmentally friendly energy sources.[83] Thermoelectric materials show great promise due to their distinctive capability of converting waste heat to one of the most abundant yet underutilized energy sources directly into electricity. Recovering this heat can substantially enhance the efficiency of industrial operations while lowering overall energy consumption. Thermoelectric generators that exploit waste heat are increasingly recognized as a sustainable pathway for future clean energy technologies. In this study, the thermoelectric characteristics of Cs_2CuLuY_6 (Y = Br, I), a family of double perovskite compounds, were explored. In essence, the study focused on how these materials can transform thermal energy into

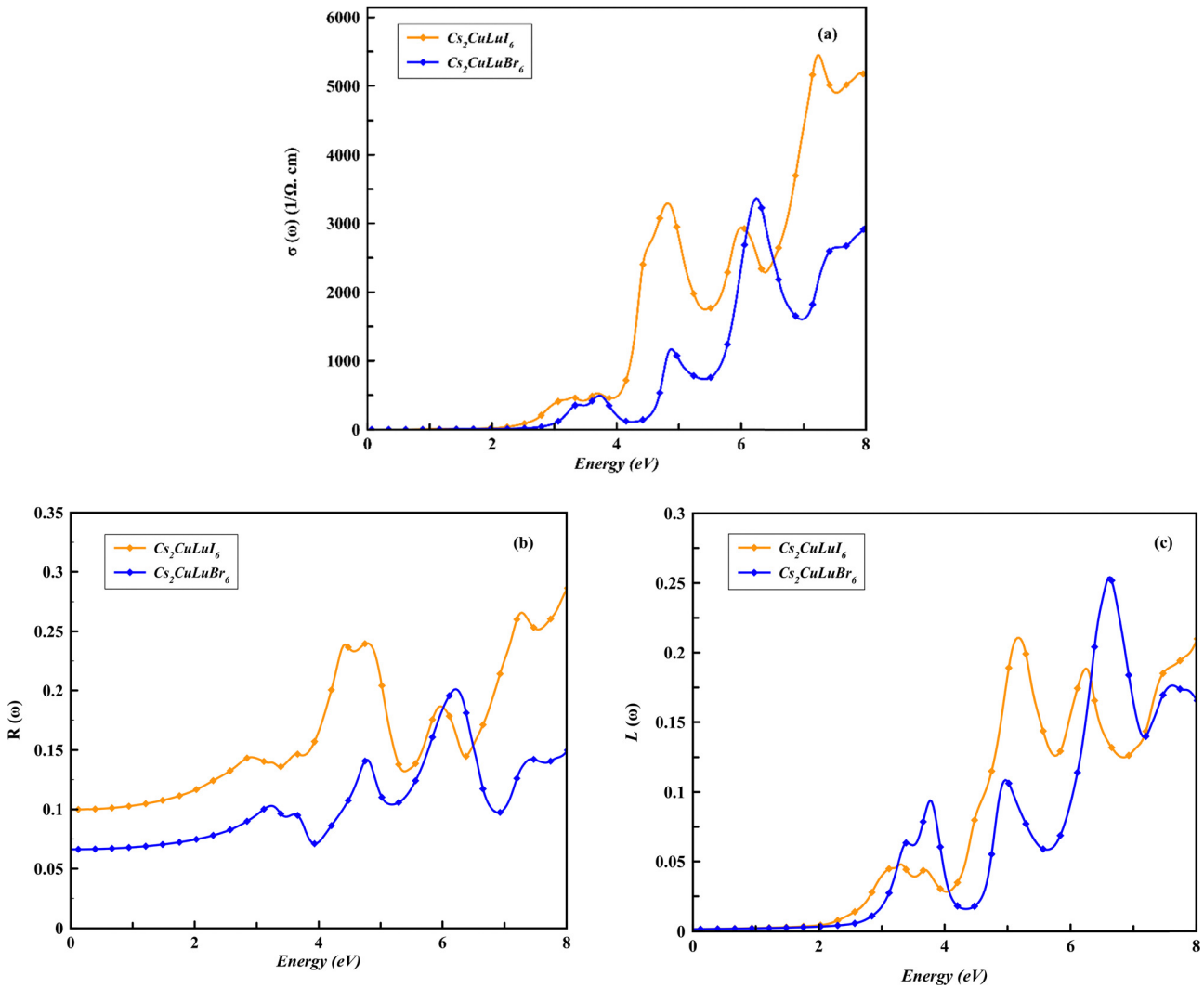

Fig. 8 (a) $\sigma(\omega)$: real optical conductivity, (b) $R(\omega)$: optical reflectivity, and (c) E_{loss}: electron energy loss of the compound.

electrical power through simulations that model electron transport under external forces. A key parameter in this process is electrical conductivity, which determines how effectively charge carriers move within the system. The findings confirm that Cs_2CuLuY_6 (Y = Br, I) behave as a semiconductor with an indirect band gap. This means the points of lowest energy in the conduction band[84] and highest energy in the valence band (minimum and maximum, respectively) occur at different locations within the material's Brillouin zone. Because the valence and conduction band edges occur at different momentum points, electrons transitioning between them require assistance from lattice vibrations (phonons) to satisfy momentum conservation. Such an indirect transition feature is typically regarded as advantageous for thermometric applications. To analyze these materials' potential for thermoelectric applications, we used the BoltzTraP2 code,[85,86] which is based on Boltzmann transport theory. This code estimated properties like electronic thermal conductivity (k_e), electrical conductivity (σ), power factor (PF), and Seebeck coefficient (S). It assumes a constant relaxation time (10^{-14} seconds) for electrons. We calculated the lattice thermal conductivity (k_L) using the Slack equation because BoltzTraP2 has limitations in this area. Finally, we combined the electronic and lattice contributions (k_L) to determine the overall thermal conductivity (k) and calculate the figure of merit (ZT) for these compounds.

3.4.1 Electrical conductivity. The electrical conductivity (σ) of the studied materials is plotted in Fig. 9(a) across a temperature range of 0 K to 1200 K. As the temperature rises, so does the electrical conductivity. This behavior is characteristic of semiconductors, where higher temperatures elevate the kinetic energy of electrons, making them more efficient conductors. Additionally, electrical conductivity is directly related to the charge carrier concentration, as expressed by the following equation:[87]

$$\sigma = ne\mu \quad (16)$$

where e is an electronic charge, and μ is mobility. The rise in σ is attributed to the augmentation of N as temperature

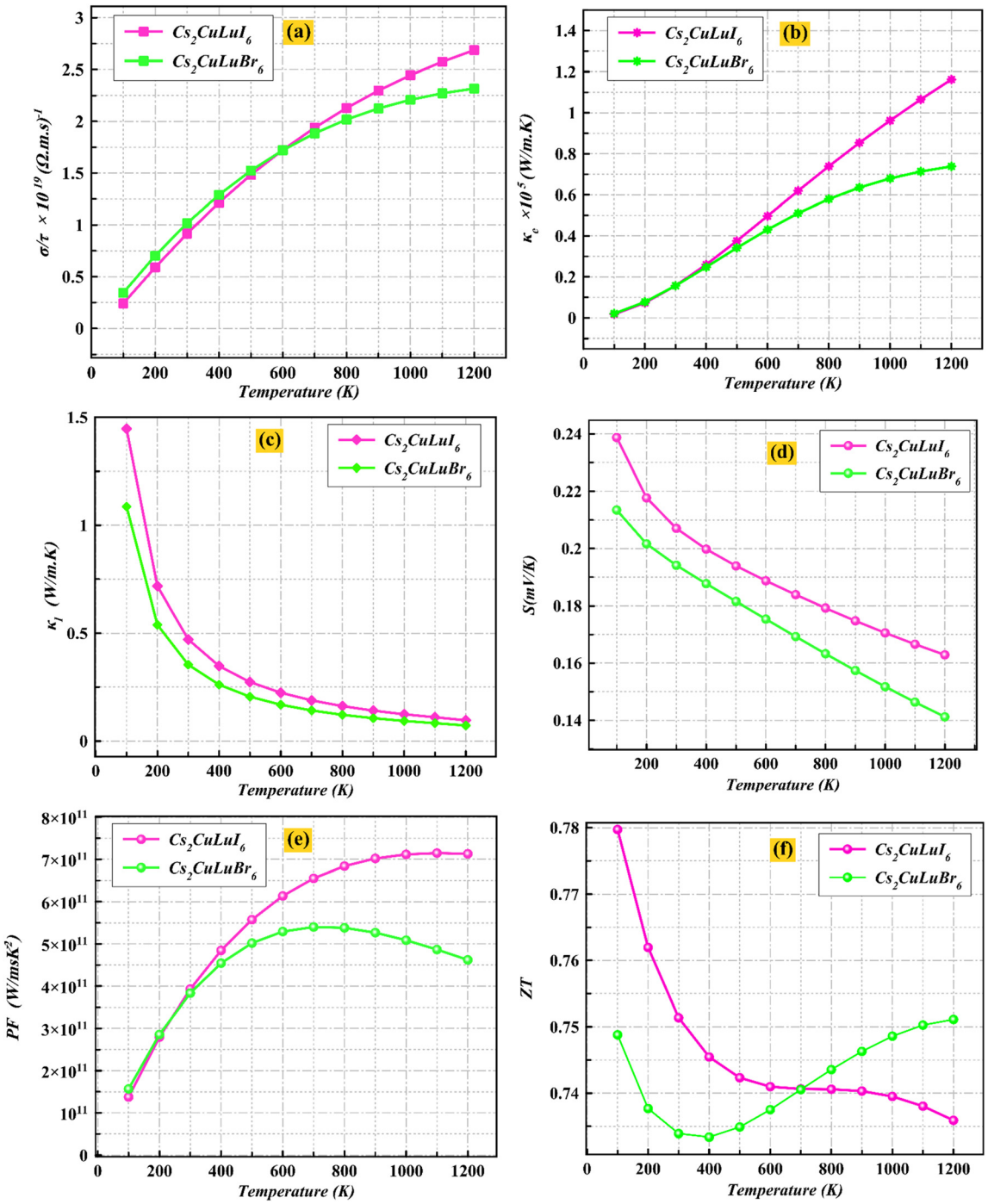

Fig. 9 (a) σ: electrical conductivity, (b) k_e: electronic conductivity, (c) k_L: thermal conductivity, (d) S: Seebeck coefficient, (e) PF: power factor, and (f) ZT: figure of merit without phonon contribution of the studied material.

increases, as shown in Fig. 9(a). Between 100 K and 1200 K, $Cs_2CuLuBr_6$ exhibits a nearly identical rise in electrical conductivity. However, $Cs_2CuLuBr_6$ shows an increase up to around 500 K, after which its conductivity begins to decline. In contrast, Cs_2CuLuI_6 displays a gradual increase from about 300 K up to 1200 K.

For $Cs_2CuLuBr_6$, the conductivity begins at 0.50×10^{19} $(\Omega\ \mathrm{ms})^{-1}$ at 300 K, reaches a peak of 0.98×10^{19} $(\Omega\ \mathrm{ms})^{-1}$ at 500 K, and then decreases with further heating. On the other hand, Cs_2CuLuI_6 shows a conductivity of 0.00×10^{19} $(\Omega\ \mathrm{ms})^{-1}$ at 100 K, gradually increasing to 0.50×10^{19} $(\Omega\ \mathrm{ms})^{-1}$ at 1200 K. Additionally, electrical conductivity exhibits a strong correlation with temperature. At high temperatures, two phenomena come into play: bond cleavage and the presence of highly energetic electrons. Bond cleavage within the material creates additional free carriers, while the increased thermal energy excites existing electrons, making them move more freely. Both factors contribute significantly

to the observed rise in σ. This emphasizes the combined effect of increased carrier concentration (N) and mobility (μ) due to temperature, ultimately leading to a stronger relationship between σ and temperature. It also connects this concept to thermoelectric performance, suggesting that this behavior could be beneficial at elevated temperatures.

3.4.2 Thermal conductivity. Thermal conductivity (k) is another critical parameter for thermoelectric materials. It represents a material's ability to conduct heat, and it can be divided into contributions from electrons (k_e) and phonons (k_L), where $k = k_e + k_L$. The electronic component (k_e) is related to electrical conductivity (σ) through the Widemann–Franz law ($k_e = L\sigma T$, where L is the Lorentz number and T is absolute temperature). The analysis of electronic conductivity (k_e) also supports the semiconducting nature of these materials, as shown in Fig. 9(b).

Fig. 9(c) shows the lattice or phonon thermal conductivity (k_L) of Cs_2CuLuY_6 (Y = Br, I) across the temperature range for both materials. These can be calculated by the popular Slack's equation, which is:

$$k_L = \frac{A\theta_D{}^3 V^{\frac{1}{3}} m}{\gamma^2 \bar{N}^{\frac{2}{3}} T} \quad (17)$$

Here, A is a constant, δ denotes the cube root of the average atomic volume, M_{av} represents the average atomic mass, θ_D refers to the Debye temperature, γ is the Grüneisen parameter, $\bar{N}$ indicates the number of atoms per unit cell, and T stands for the absolute temperature measured in Kelvin. At 1200 K, Cs_2CuLuI_6 exhibits the highest thermal conductivity, reaching 1.18×10^{15} W m^{-1} K^{-1}. In contrast, $Cs_2CuLuBr_6$ shows a much lower value of 0.10×10^{15} W m^{-1} K^{-1} at 500 K.

Notably, both materials experience a significant drop in k_L values at higher temperatures, reaching values of 0.021 W m^{-1} K^{-1} for Cs_2CuLuI_6 and $Cs_2CuLuBr_6$, respectively, at 1200 K. These low lattice thermal conductivity values are favorable for thermoelectric devices.[88] These values indicate that Cs_2CuLuY_6 can efficiently impede heat flow within the material, allowing a larger temperature difference to be maintained across the device. This temperature difference is crucial for thermoelectric conversion efficiency.

3.4.3 Seebeck coefficient. The Seebeck coefficient (S), a measure of a material's thermometric properties, is plotted in Fig. 9(d) for Cs_2CuLuY_6 (Y = Br, I). When a temperature gradient is established across a material, it induces the generation of an electromotive force (emf),[89] as indicated by the positive Seebeck coefficient values (0.50 mV K^{-1} for Cs_2CuLuI_6 and 0.18 mV K^{-1} for $Cs_2CuLuBr_6$ at 300 K). Such a trend is typical for p-type semiconductors, in which holes act as the primary charge carriers. Notably, the Seebeck coefficient remains positive across the studied temperature interval (100 K to 1200 K), but its value gradually declines as temperature rises. This reduction indicates a delicate balance between carrier density and thermal effects, ultimately influencing the thermoelectric efficiency of the material.

$$S = \left(\frac{8\pi^2 {k_B}^2}{3h^2 e}\right)\left(\frac{\pi}{3N}\right)^{\frac{2}{3}} m^* T \quad (18)$$

The observation of a positive Seebeck coefficient is consistent with earlier reports, where the electronic band structure places the Fermi level (E_F) near the top of the valence band,[90] thereby reinforcing the p-type nature of these compounds.

3.4.4 Power factor. The power factor (PF) serves as an essential indicator for evaluating the potential of materials in thermoelectric applications. It reflects a balance between electrical conductivity (σ) and the Seebeck coefficient (S), which represents the ability to convert heat into electrical energy. Mathematically expressed as PF = $S^2\sigma$, a higher value indicates better thermoelectric efficiency. Literature suggests that a PF of 1 or greater is generally regarded as favorable for practical thermoelectric devices.[91] Fig. 9(e) represents the temperature dependence of the power factor for Cs_2CuLuY_6 (Y = Br, I). Interestingly, the trend reveals an opposing effect between S and σ. While the Seebeck coefficient decreases with increasing temperature, electrical conductivity increases. This interplay significantly impacts the overall power factor. The low/high-temperature power factor values are $0.00/2 \times 10^{11}$ W ms^{-1} K^{-1} and for Cs_2CuLuI_6, $1.50\ 10^{11}/0.5 \times 10^{11}$ W ms^{-1} K^{-1} for $Cs_2CuLuBr_6$. The findings indicate that the examined compounds exhibit strong potential for thermoelectric applications, especially under high-temperature conditions.

3.4.5 Figure of merit. The thermoelectric performance of a material is commonly evaluated using the figure of merit (ZT), a dimensionless quantity that measures its overall efficiency. The figure of merit depends on a material's electrical conductivity (σ), Seebeck coefficient (S), and thermal conductivity (k). In several studies, researchers have focused primarily on the electronic part of this parameter, which can be expressed as:

$$ZT = \frac{S^2\sigma}{k_e} T \quad (19)$$

Fig. 9(f) shows the ZT value beyond the lattice or phonon contribution, where this value decreases and increases with increasing temperature. Using this approach, the calculated ZT values were found to be 0.99 at 100 K and 0.92 at 1200 K for Cs_2CuLuI_6, and 0.68 at 100 K and 0.69 at 1200 K for $Cs_2CuLuBr_6$. In comparison, Cs_2CuLuI_6 exhibits higher ZT values than the $Cs_2CuLuBr_6$, primarily due to its very low lattice thermal conductivity (k_L). These outcomes highlight the promise of Cs_2CuLuY_6 compounds for thermoelectric device applications, especially under ambient conditions. It is worth noting that lattice thermal conductivity estimated using Slack's equation often yields larger values compared to approaches like the BTE method. Therefore, it can be expected that the actual ZT values will be greater than those calculated here, reinforcing the potential of the examined double-halide perovskites as strong candidates for thermoelectric technologies.

3.4.6 The Seebeck coefficient as a function of chemical potential. The Seebeck coefficient (S) of Cs_2CuLuY_6 (Y = Br, I) is

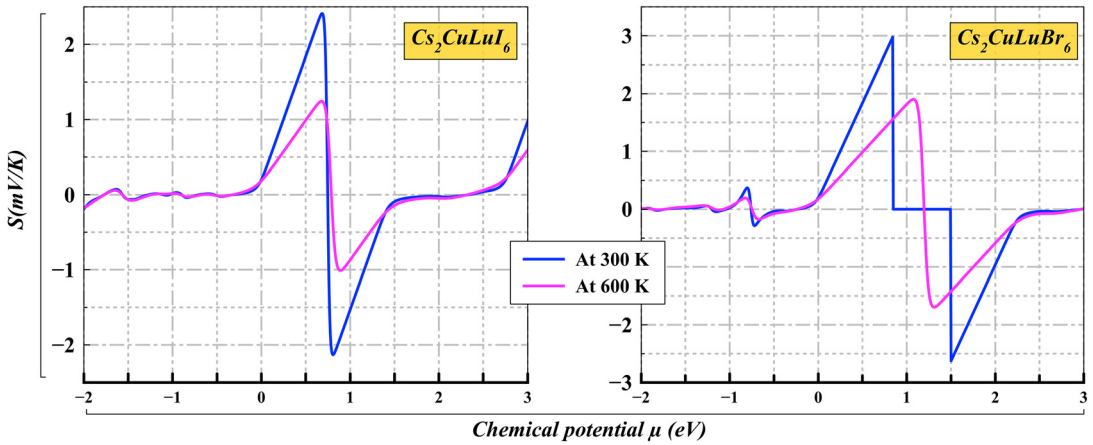

Fig. 10 Relationship between chemical potential and Seebeck coefficient of Cs_2CuLuY_6 (Y = Br, I).

evaluated using the ratio of voltage (V) to the applied temperature gradient (ΔT), expressed as $\Delta S = V/\Delta T$. The correlation between chemical potential and variations in S is illustrated in Fig. 10(a)–(d) for Cs_2CuLuI_6 and $Cs_2CuLuBr_6$. A positive S value signifies that holes dominate as charge carriers, whereas a negative S reflects electron-driven transport. For the n-type phases of Cs_2CuLuI_6 and $Cs_2CuLuBr_6$, the coefficient remains negative, while the p-type counterparts exhibit positive values. At room temperature, the Seebeck coefficient values for the p-type variants are approximately 3.0 and 2.5 mV K^{-1}, respectively.

The results further reveal that S attains its maximum near 300 K, followed by a noticeable decline at around 600 K. For the n-type compounds, the magnitude of S consistently decreases with rising temperature. Overall, the studied materials display a clear dominance of p-type carriers, as evidenced by their comparatively larger S values relative to n-type carriers, whose contribution weakens at elevated temperatures. This behavior arises because, at lower temperatures, these semiconductors possess a limited number of intrinsic carriers. As the thermal energy increases, more electrons are excited into the conduction band, reducing the Seebeck coefficient accordingly.[92]

3.4.7 Relationship between chemical potential and electrical conductivity. In semiconductors, electrical conductivity arises from the combined contribution of both electrons and holes. Fig. 11(a)–(d) depict how conductivity varies with chemical potential at different temperatures. The results reveal that Cs_2CuLuI_6 display a steady increase in conductivity as the temperature rises, whereas $Cs_2CuLuBr_6$ exhibit a decreasing trend with higher temperatures. The maximum conductivity values are 15.6 × 10^{19} and 15.3 × 10^{19} $(\Omega\ ms)^{-1}$ at 300 K and 600 K for Cs_2CuLuI_6 at −1.8 eV; and 10.2 × 10^{19} and 9.2 × 10^{19} $(\Omega\ ms)^{-1}$ at 300 K and 600 K for $Cs_2CuLuBr_6$ at 3.5 eV.

3.5. Thermo-mechanical properties

The determination of the elastic constants C_{11}, C_{12}, and C_{44} for cubic alloys is crucial for understanding their mechanical stability, bonding nature, ductility, and overall mechanical behavior as well as how they respond to externally applied forces. For cubic crystals, these constants satisfy the relationships: $C_{11} = C_{22} = C_{33}$, $C_{12} = C_{32} = C_{13}$, and $C_{44} = C_{55} = C_{56}$. Mechanical stability requires satisfying the Born stability criteria:[93] $C_{11} - 2C_{12} > 0$, $C_{44} > 0$, $C_{11} > B > C_{12}$ and $C_{11} - C_{12} > 0$. Our calculations confirm these criteria, indicating the mechanical stability of the Cs_2CuLuY_6 (Y = Br, I). Additionally, both computed elastic constants are positive, so a Born–Huang stability criterion for Cs_2CuLuY_6 is completely justified.

Mechanical properties such as shear modulus, Cauchy pressure, bulk modulus, Young's modulus, Poisson's ratio, Pugh's ratio, and anisotropic ratio are essential for assessing material performance displayed in the table. For Cs_2CuLuY_6 (Y = Br, I), the bulk modulus (B), shear modulus (G), and Young's modulus (Y) indicate resistance to volume, shear, and longitudinal deformation, respectively. A higher bulk modulus than a shear modulus shows better deformation resistance, and a high Young's modulus indicates stiffness.

Cauchy pressure ($C_p = C_{12} - C_{44}$) and Pugh's ratio are used to determine ductility or brittleness: a positive Cauchy pressure along with a Pugh's ratio exceeding 1.75 signifies ductile behavior. Our materials, Cs_2CuLuY_6 (Y = Br, I), are ductile with Cauchy pressure and Pugh's ratio values. Poisson's ratio (σ) values above 0.26 also indicate ductility, as seen in our materials with σ in Table 4. Materials with lower Poisson's ratio (σ) values exhibit higher stability under shear stress.

Table 4 presents the evaluated hardness values. The H_v for Cs_2CuLuI_6, and $Cs_2CuLuBr_6$ are 1.74 GPa and 2.32 GPa, respectively. These materials are considered soft compared to diamonds, which have hardness values ranging from 70 to 150 GPa.[94]

A material is isotropic if the anisotropy index (A) equals 1, and anisotropic if A is either less than or greater than 1.[95] By examining the variation of physical properties and elasticity in both 2D and 3D representations, we can grasp the concept of anisotropy. If they are perfectly circular in 2D or spherical in 3D, they are isotropic. Otherwise, they are anisotropic. As a result, the assessed value of Cs_2CuLuY_6 (Y = Br, I) shows that all compounds exhibit anisotropic behavior (Table 4 and Fig. 15). Fig. 12 and 13 demonstrate the directional variation of Young's modulus (Y), shear modulus (G), and Poisson's ratio (ν) for the Cs_2CuLuY_6 (Y = Br, I).

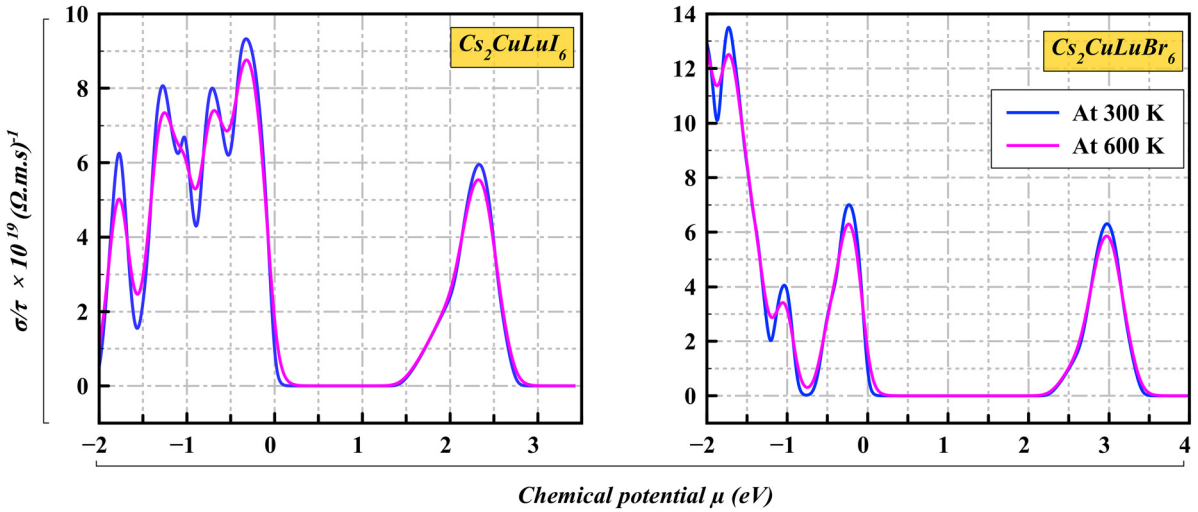

Fig. 11 Relationship between chemical potential and electrical conductivity of Cs_2CuLuY_6 (Y = Br, I).

Table 4 Elastic parameters and mechanical stability of studied compounds with reference materials

Elastic constant	Cs_2CuLuI_6	$Cs_2CuLuBr_6$	Cs_2GeZnI_6[33]	$Cs_2CdBeCl_6$[35]	$Cs_2SnBeCl_6$[35]
C_{11} (GPa)	38.62	48.86	30.67	47.38	44.93
C_{12} (GPa)	13.56	18.97	9.60	24.41	19.27
C_{44} (GPa)	10.57	15.13	9.83	23.42	17.72
B (GPa)	21.91	28.94	16.62	32.07	27.82
G (GPa)	11.31	15.05	10.11	17.59	15.56
Y (GPa)	28.95	38.49	25.22	44.60	39.36
B/G	1.93	1.86	1.64	1.82	1.78
σ	0.27	0.27	0.24	0.26	0.26
$C_p = C_{12} - C_{44}$	2.99	3.84	−0.23	0.99	1.55
$\mu = B/C_{44}$	2.07	1.91	—	—	—
ξ	0.49	0.52	—	—	—
H	1.74	2.32	—	—	—
A	0.84	1.01	0.94	2.03	1.38
Elastic Debye temperature, θ_D (k)	143.23	180.47	—	—	—
Transverse sound velocity, V_t (m s^{-1})	1495.77	1748.16	—	2187.25	2148.62
Longitudinal sound velocity, V_l (m s^{-1})	2705.16	3154.02	—	3885.77	3795.55
Averaged sound velocity, V_{av} (m s^{-1})	1666.54	1947.38	—	2431.60	2387.53
Melting point, T_m (± 300 K)	781.24 ± 300	841.81 ± 300	734.28 ± 300	833.01 ± 300	818.54 ± 300
Mini. thermal conductivity, K_{min} (W m^{-1} K^{-1})	0.23	0.29	—	—	—

The Kleinman parameter (ξ), typically ranging from 0 to 1, measures resistance to stretching and bending. It is 0.49 for Cs_2CuLuI_6 and 0.52 for $Cs_2CuLuBr_6$ (Table 4), suggesting strong mechanical properties and minimal bond stretching (Fig. 14).[96]

Elastic constants serve as useful parameters for estimating a material's melting point and Debye temperature. Atomic vibrations in a crystal lattice can be viewed as sound waves, and the Debye temperature represents the point at which atomic vibrations within a solid become fully active. The computed Debye temperature (θ_D) values can be arranged in the following sequence: $Cs_2CuLuBr_6$ > Cs_2CuLuI_6, and the average sound velocity (V_{av} follows the same trend as the Debye temperature). Higher Debye temperatures can impact energy conversion efficiency by strengthening atomic bonds and improving thermal stability. The ultrasonic wave velocities in the double perovskite materials are determined using solid-state electrochemical cell techniques. The longitudinal (V_l) and transverse (V_t) sound velocities are used to calculate the average sound velocity (V_{av}). The melting temperature is the point at which a substance transitions from a solid to a liquid. Materials with higher melting temperatures have stronger atomic interactions and greater bonding energies. Based on the results, the materials exhibit these characteristics in the following order: $Cs_2CuLuBr_6$ > Cs_2CuLuI_6. The Cahill formula is also utilized to estimate the minimum thermal conductivity (K_{min}).[97] Low thermal conductivity reduces internal heat buildup, helping to prevent material degradation and improve overall efficiency. Double perovskites possessing low thermal conductivity can enhance power conversion efficiency in solar cells by minimizing heat loss and facilitating the transformation of waste heat into usable energy. $Cs_2CuLuBr_6$ > Cs_2CuLuI_6 as minimum thermal conductivity (K_{min}).

Fig. 15 illustrates the variation of Helmholtz free energy (G), internal energy (U), entropy (S), and heat capacity (C_V) with temperature. As observed, the free energy decreases steadily as temperature rises, whereas both internal energy and heat

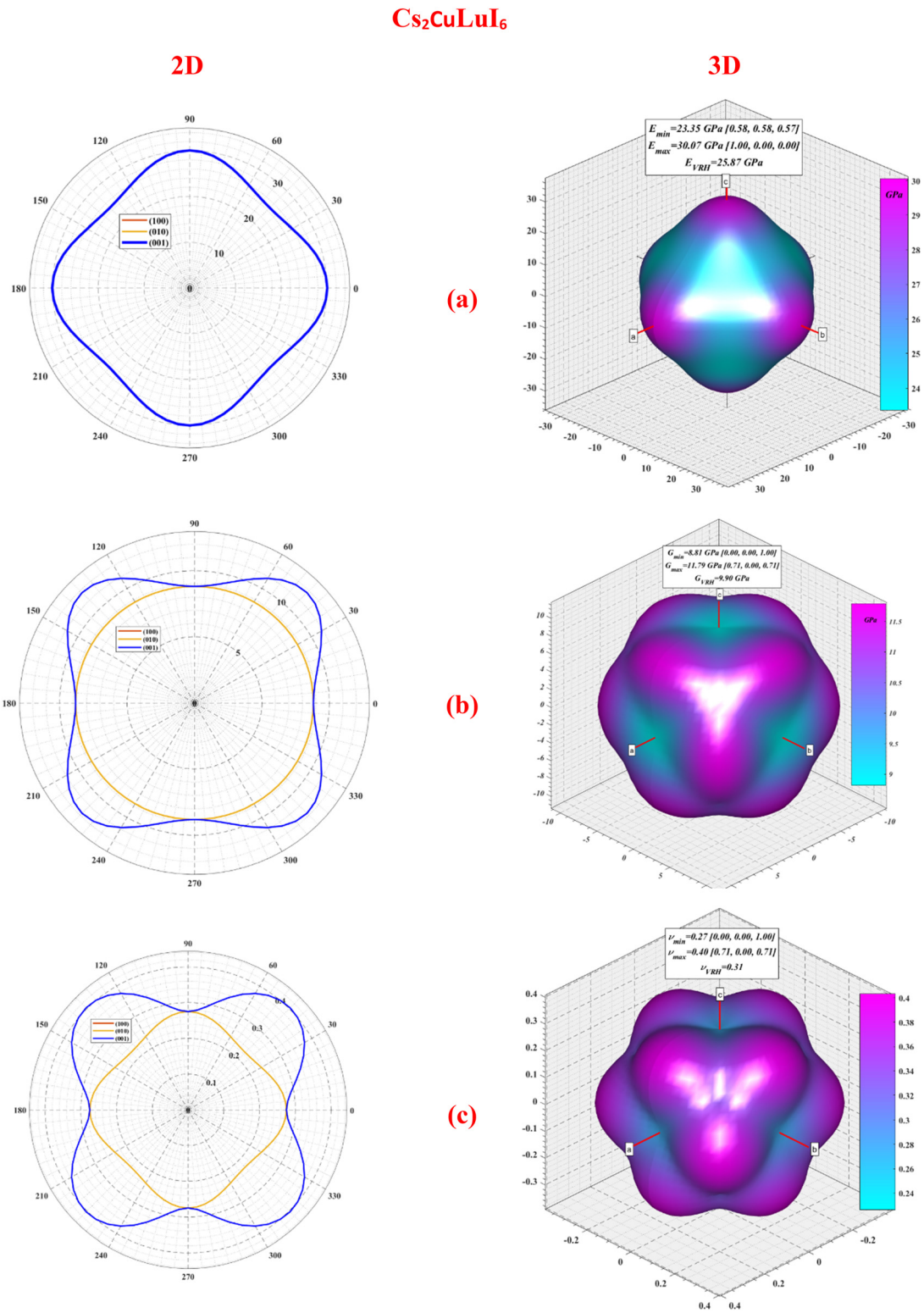

Fig. 12 (a) Young's modulus (Y), (b) shear modulus (G), and (c) Poisson's ratio (ν) for Cs_2CuLuI_6, showing the 2D and 3D anisotropic representations.

capacity show an increasing trend for the studied compounds. Entropy, however, exhibits a sharp rise from 0 K to 100 K, after which it remains nearly constant. These thermodynamic parameters were determined at zero pressure using the quasi-harmonic approximation (QHA). From the plots, it is evident that at very low temperatures, the free energy (G), internal energy (U), and heat capacity (C_V) are nearly zero. In contrast, the initial entropy (S) values for Cs_2CuLuI_6 and $Cs_2CuLuBr_6$ are approximately −630 and

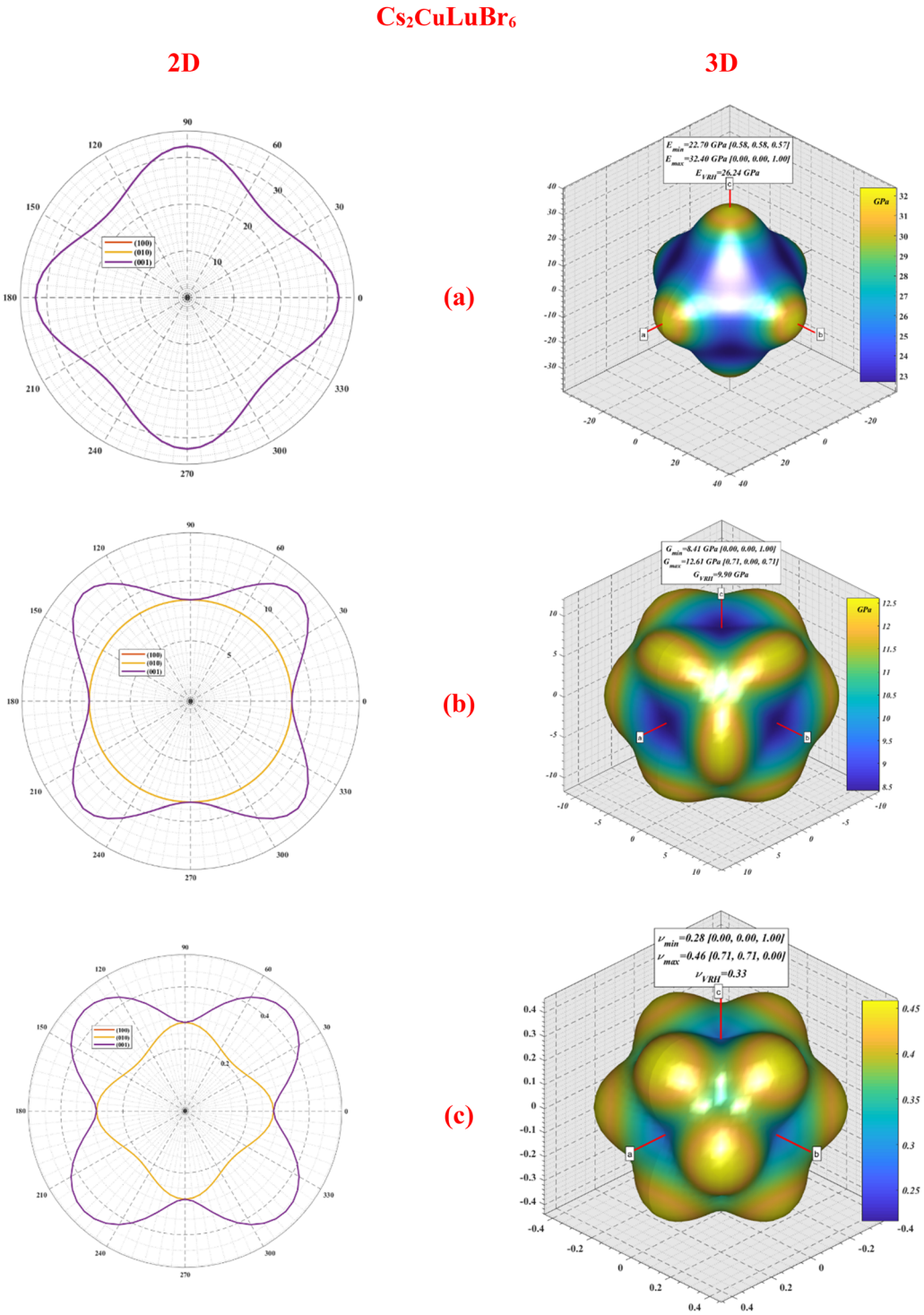

Fig. 13 (a) Young's modulus (Y), (b) shear modulus (G), and (c) Poisson's ratio (ν) for $Cs_2CuLuBr_6$, showing the 2D and 3D anisotropic representations.

−710 kJ mol^{-1}, respectively. Since negative free energy values are indicative of thermodynamic stability,[98] all investigated double perovskites can be considered stable under the studied conditions. Additionally, Fig. 15 highlights the entropy behavior, which reflects the system's thermal energy. At 0 K, the entropy of all compounds is zero, but it increases with temperature as atomic vibrations become more pronounced. The entropy reaches a maximum of about 100 J K^{-1} mol^{-1} at 100 K and then levels off. Likewise, the heat capacity (C_V) increases almost linearly with temperature, attaining a peak of ∼400 J K^{-1} mol^{-1} at 1200 K for all the

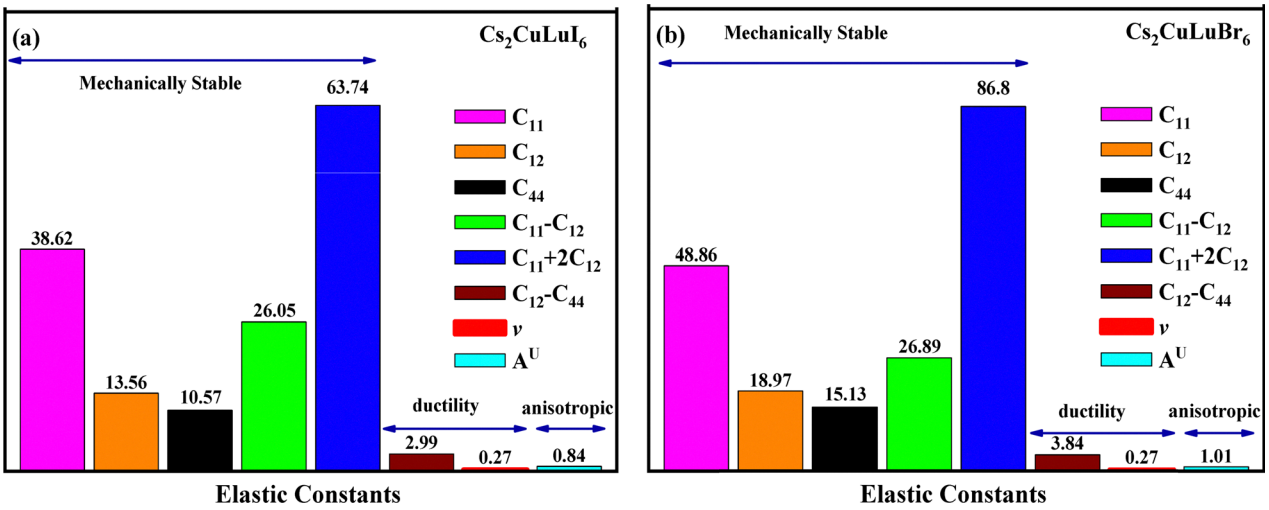

Fig. 14 Mechanical stability, ductility, and anisotropy of (a) Cs_2CuLuI_6 and (b) $Cs_2CuLuBr_6$.

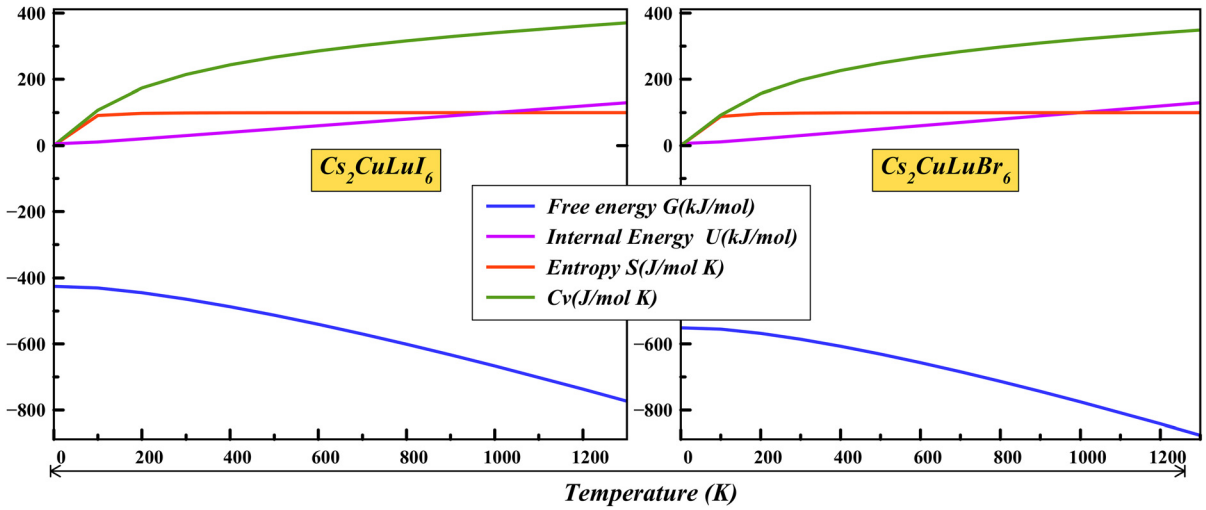

Fig. 15 Free energy (G), entropy (S), and heat capacity (C_V) thermal curves.

compounds. Table 4 clearly shows that the calculated properties of our studied material are in close agreement with previously reported Cs-based reference materials, thereby validating the accuracy and reliability of our present study.

Overall, these findings confirm that Cs_2CuLuY_6 perovskites exhibit excellent thermodynamic stability and are therefore suitable for a broad range of technological applications.

4. Conclusion

In this study, the structural, electronic, optical, thermo-mechanical, and thermoelectric properties of Cs_2CuLuY_6 (Y = Br, I) double perovskites were systematically explored using density functional theory (DFT). Structural stability was verified through tolerance factors, octahedral factors, modified tolerance factor, formation energy, and thermodynamic analysis *via* Helmholtz free energy, entropy, and heat capacity. Phonon dispersion results reveal the absence of imaginary frequencies, confirming the dynamical stability of these compounds. The calculated elastic constants fulfilled Born's stability criteria, while Poisson's ratio and Pugh's ratio confirmed the ductile characteristics of these compounds. The anisotropy index further revealed their anisotropic nature. Electronic structure analysis confirms that Cs_2CuLuY_6 compounds exhibit indirect band gaps and semiconducting behavior. The obtained band gap range lies within the favorable window for visible-light absorption, indicating their potential for light-harvesting and optoelectronic applications. Optical investigations revealed strong absorption extending from the visible to ultraviolet region, with relatively low reflectivity and high refractive index, making them suitable for applications in solar absorbers, LEDs, and photonic devices. Thermoelectric analysis indicated that Cs_2CuLuI_6 exhibits the highest figure of merit (ZT = 0.99 at 100 K and 0.92 at 1200 K), attributed to its low lattice thermal conductivity, whereas $Cs_2CuLuBr_6$ also exhibits moderate

thermoelectric potential. The Seebeck coefficient values confirmed p-type semiconducting behavior, with significant contributions from hole carriers across the studied temperature range. Together, these findings establish Cs_2CuLuY_6 perovskites as multifunctional materials with potential for energy-harvesting. Their combined optoelectronic and thermoelectric capabilities highlight Cs_2CuLuY_6 as a promising candidate for next-generation renewable energy applications.

Author contributions

Md Shahazan Parves: investigation, methodology, data curation, conceptualization, writing original manuscript, supervision. Rashel Mohammad Khokan: formal analysis, validation, review – editing. Md. Zahid Hasan: formal analysis, validation, review – editing. Hadjer BENDJILALI: methodology, conceptualization, data curation, investigation, review – editing, supervision.

Conflicts of interest

There are no conflicts to declare.

Data availability

The data supporting this study are available from the corresponding author upon reasonable request.

Acknowledgements

No funding was received for conducting this study.

References

1 M. A. Ali, *et al.*, Electronic, Optical and Thermoelectric Properties of Stable A_2LiIO_6 (A = Sr, Ba) Lead-Free Double Perovskites for Low-Cost Energy Applications, *J. Inorg. Organomet. Polym. Mater.*, 2024, **34**(7), 3270–3280.
2 W. Zhang, *et al.*, Metal halide perovskites for energy applications, *Nat. Energy*, 2016, **1**(6), 1–8.
3 W.-J. Yin, *et al.*, Unique properties of halide perovskites as possible origins of the superior solar cell performance, *Adv. Mater.*, 2014, **26**(27), 4653–4658.
4 A. Bibi, *et al.*, Lead-free halide double perovskites: Toward stable and sustainable optoelectronic devices, *Mater. Today*, 2021, **49**(11), 123–144.
5 W.-J. Yin, *et al.*, Halide perovskite materials for solar cells: a theoretical review, *J. Mater. Chem. A*, 2015, **3**(17), 8926–8942.
6 J. Song, *et al.*, Quantum Dot Light-Emitting Diodes Based on Inorganic Perovskite Cesium Lead Halides ($CsPbX_3$), *Adv. Mater.*, 2015, **27**(44), 7162–7167.
7 S. A. Veldhuis, *et al.*, Perovskite Materials for Light-Emitting Diodes and Lasers, *Adv. Mater.*, 2016, **28**(32), 6804–6834.
8 H. Murtaza, *et al.*, Scrutinize the physical attributes of thermodynamically and elastically stable double perovskite oxides Ba_2CdXO_6 (X= Mo, U) for optoelectronics, photocatalytic and green technology, *Comput. Mater. Sci.*, 2024, **232**, 112674.
9 A. Kojima, *et al.*, Organometal Halide Perovskites as Visible-Light Sensitizers for Photovoltaic Cells, *J. Am. Chem. Soc.*, 2009, **131**(17), 6050–6051.
10 F. Bella, *et al.*, Improving efficiency and stability of perovskite solar cells with photocurable fluoropolymers, *Science*, 2016, **354**(6309), 203–206.
11 L. Chu, *et al.*, High-performance large-area perovskite photovoltaic modules, *Nano Res. Energy*, 2022, **1**(2), e9120024.
12 A. Babayigit, *et al.*, Assessing the toxicity of Pb-and Sn-based perovskite solar cells in model organism Danio rerio, *Sci. Rep.*, 2016, **6**(1), 18721.
13 M. T. Anderson, *et al.*, B-cation arrangements in double perovskites, *Prog. Solid State Chem.*, 1993, **22**(3), 197–233.
14 M. A. Khan, *et al.*, Comprehensive investigation of Optoelectronic and transport properties of Cs_2ScAgX_6 (X = Cl, Br, I) for solar cells and thermoelectric applications, *Sol. Energy*, 2021, **225**, 122–128.
15 M. R. Jani, *et al.*, Exploring solar cell performance of inorganic Cs_2TiBr_6 halide double perovskite: A numerical study, *Superlattices Microstruct.*, 2020, **146**, 106652.
16 D. Abdullah, *et al.*, Exploring the structural, Mechanical, electronic, optical, and thermoelectric properties of Cesium-based double perovskite Cs_2GeSnX_6 (X = Cl, Br, I) compounds: A DFT study, *Mater. Sci. Semicond. Process.*, 2023, **167**, 107813.
17 S. M. Qaid, *et al.*, Investigation of the amplified spontaneous emission threshold of cesium lead bromide perovskite quantum dots at different excitation wavelengths, *ECS J. Solid State Sci. Technol.*, 2023, **12**(5), 055012.
18 S. Berri, *et al.*, Thermoelectric properties of A_2BCl_6: a first-principles study, *J. Phys. Chem. Solids*, 2022, **170**, 110940.
19 S. Berri, *et al.*, First-principles calculations to investigate structural, electronic, elastic, optical and transport properties of halide double perovskites Cs_2ABF_6 (AB = BiAu, AgIr, CuBi, GaAu, InAs, InAg, InAu, InSb and InBi) for solar cells and renewable energy applications, *Chem. Phys. Lett.*, 2023, **826**, 140653.
20 S. Berri, *et al.*, First-principles studies of thermoelectric and thermodynamic properties of the complex perovskite $Ba_3MnNb_2O_9$, *J. Sci. Adv. Mater. Devices*, 2020, **5**(3), 378–384.
21 S. Berri, *et al.*, Ab-initio calculations on structural, electronic, half-metallic and optical properties of Co-, Fe-, Mn- and Cr-doped B_2LuTaO_6, *Pramana*, 2021, **95**(1), 38.
22 W. Zheng, *et al.*, First Principle Study of Cesium-based Lead-free Halide Double Perovskites, *J. Wuhan Univ. Technol., Mater. Sci. Ed.*, 2023, **38**(3), 520–529.
23 A. H. Slavney, *et al.*, A Bismuth-Halide Double Perovskite with Long Carrier Recombination Lifetime for Photovoltaic Applications, *J. Am. Chem. Soc.*, 2016, **138**(7), 2138–2141.
24 H. Saci, *et al.*, Optoelectronic properties and lattice thermal conductivity of Cs_2CuBiX_6 (X = F, Cl, Br, I) double perovskites: Thermodynamic and ab initio approaches, *Sci. Direct*, 2024, **35**, e00791.

25 M. Caid, *et al.*, Theoretical insight of stabilities and optoelectronic properties of double perovskite Cs_2CuIrF_6: Ab-initio calculations, *J. Mol. Model.*, 2023, **29**(6), 178.
26 M. G. B. Ashiq, *et al.*, The narrow band bap double perovskites $X_2CuInCl_6$ (X = K, Rb, Cs) for optoelectronics, and thermoelectric applications, *Mater. Sci. Eng., B*, 2023, **296**, 116690.
27 D. Behera, *et al.*, First-principle investigations on optoelectronics and thermoelectric properties of lead-free Rb_2InSbX_6 (X = Cl, Br) double perovskites: for renewable energy applications, *Eur. Phys. J. Plus*, 2023, **138**(6), 520.
28 K. Assiouan, *et al.*, Theoretical investigation of Rb_2AuBiX_6 (X = Br, Cl, F) double perovskite for thermoelectric and optoelectronic applications, *J. Phys. Chem. Solids*, 2024, **188**, 111890.
29 A. Boutramine, *et al.*, First-principles investigation of K_2InSbZ_6 (Z = I, Br, Cl, F) eco-friendly halide double perovskites: Structural, thermodynamic, optoelectronic, and thermoelectric properties for efficient energy harvesting applications, *Phys. B*, 2025, **711**, 417280.
30 A. Es-Smairi, *et al.*, DFT Insights Into the Structural, Stability, Elastic, and Optoelectronic Characteristics of Na_2 $LiZF_6$ (Z = Ir and Rh) Double Perovskites for Sustainable Energy, *J. Comput. Chem.*, 2025, **46**(8), e70097.
31 M. Caid, *et al.*, Physical characteristics of Pb_2FeSbO_6 double perovskite for thermoelectric applications, *Phys. B*, 2025, **707**, 417192.
32 M. Caid, *et al.*, Pb_2CoMoO_6 as a Promising Energy Material: A First-Principles Perspective, *J. Inorg. Organomet. Polym. Mater.*, 2026, **36**(1), 748–765.
33 M. Caid, *et al.*, DFT assessment on the future prospects of inorganic lead-free halide double perovskites Cs_2ABI_6 (AB: GeZn, SnBe) for energy conversion technologies, *Comput. Condens. Matter*, 2024, **41**, e00978.
34 S. Al-Qaisi, *et al.*, Comprehensive DFT study of K_2TlZI_6 (Z= Al, In) double perovskites: Structural stability and potential for optoelectronic and thermoelectric energy harvesting, *Phys. B*, 2025, **710**, 417239.
35 A. Benkatlane, *et al.*, Lead-Free Cs_2 (Cd/Sn) $BeCl_6$ Halide Double Perovskites: A Comprehensive First-Principles Study of Structural, Optoelectronic, and Thermoelectric Properties for Sustainable Energy Applications, *Phys. Status Solidi B*, 2026, **263**(1), e202500019.
36 H. Rached, *et al.*, Future insights into double perovskites Ba_2AlTMO_6 (TM= W, Re, and Os) for sustainable and clean energy production: a DFT investigation using GGA, TB-mBJ, and HSE06 methods, *J. Inorg. Organomet. Polym. Mater.*, 2025, **35**(7), 5239–5260.
37 H. Murtaza, *et al.*, Scrutinize the physical attributes of thermodynamically and elastically stable double perovskite oxides Ba_2CdXO_6 (X = Mo, U) for optoelectronics, photocatalytic and green technology, *Comput. Mater. Sci.*, 2024, **232**, 112674.
38 H. Murtaza, *et al.*, Exploring the optoelectronic attributes, thermoelectric and photocatalytic potential of double perovskites $Cs_2BB'H_6$ (B = Al, Na and B′ = Tl, In): A DFT study, *Mater. Sci. Eng., B*, 2024, **301**, 117171.
39 H. Murtaza, *et al.*, Tuning the thermoelectric and optoelectronic attributes of lead-free novel fluoroperovskites $Cs_2BB'F_6$ (B = Rb, In, Na and B′ = Ir, As, Rh): a first-principles investigation, *J. Phys. Chem. Solids*, 2024, **190**, 111934.
40 H. Murtaza, *et al.*, Effect of bandgap tunability on the physical attributes of potassium-based K_2CuBiX_6 (X = I, Br, Cl) double perovskites for green technologies, *Inorg. Chem. Commun.*, 2024, **162**, 112206.
41 H. Murtaza, *et al.*, Unveiling the mechanical, structural, thermoelectric, and optoelectronic potential of $K_2NaGaBr_6$ and $K_2RbTlBr_6$ double perovskites for sustainable technologies, *Solar Energy*, 2024, **273**, 112502.
42 H. Murtaza, *et al.*, A comprehensive theoretical analysis of the physical attributes of cesium-based $Cs_2LiTlCl_6$ double perovskites for eco-friendly technologies, *Phys. B*, 2024, **677**, 415729.
43 S. M. H. Qaid, *et al.*, A computational insight into Rb_2ASbX_6 (A = Tl, Cu & X = I, Cl) double perovskites for energy storage and optoelectronic applications, *Phys. Scr.*, 2023, **98**(10), 105910.
44 S. M. H. Qaid, *et al.*, A computational approach to correlate the physical attributes of lead-free Rb_2XRhF_6 (X = Li, Ag) double perovskite halides for optoelectronics and renewable energy applications, *Phys. B*, 2023, **671**, 415416.
45 J. Munir, *et al.*, First-principles investigations of the mechanically and thermodynamically stable potassium-based double perovskites K_2TlAsX_6 (X = Cl, Br) for optoelectronic and renewable applications, *Mater. Sci. Eng., B*, 2023, **298**, 116830.
46 J. Munir, *et al.*, First-principles investigations of the mechanically and thermodynamically stable potassium-based double perovskites K_2TlAsX_6 (X = Cl, Br) for optoelectronic and renewable applications, *Mater. Sci. Eng., B*, 2023, **298**, 116830.
47 K. Schwarz, *et al.*, DFT calculations of solids with LAPW and WIEN2k, *J. Solid State Chem.*, 2003, **176**(2), 319–328.
48 J. P. Perdew, *et al.*, Generalized Gradient Approximation Made Simple, *Phys. Rev. Lett.*, 1996, **77**(18), 3865–3868.
49 H. Jiang, *et al.*, Band gaps from the Tran-Blaha modified Becke-Johnson approach: A systematic investigation, *J. Chem. Phys.*, 2013, **138**(13), 134115.
50 G. K. Madsen, *et al.*, BoltzTraP2, a program for interpolating band structures and calculating semi-classical transport coefficients, *Comput. Phys. Commun.*, 2018, **231**(1), 140–145.
51 C. Li and X. Lu, *et al.*, Formability of abx_3 (x = f, cl, br, i) halide perovskites, *Acta Crystallogr., Sect. B:Struct. Sci.*, 2008, **64**(6), 702–707.
52 M. Saeed, *et al.*, First-principles prediction of the ground-state crystal structure of double-perovskite halides Cs_2AgCrX_6 (X = Cl, Br, and I), *J. Phys. Chem. Solids*, 2022, **160**(1), 110302.
53 S. A. Mir, *et al.*, Analysis of cage structured halide double perovskites Cs_2NaMCl_6 (M = Ti, V) by spin-polarised calculations, *J. Alloys Compd.*, 2021, **854**(15), 156000.

54 X. Du, *et al.*, Insights on electronic structures, elastic features and optical properties of mixed-valence double perovskites $Cs_2Au_2X_6$ (X = F, Cl, Br, I), *Phys. Lett. A*, 2020, **384**(8), 126169.
55 M. A. Bakkar Siddique, *et al.*, Exploring Optoelectronic Behavior and Solar Cell Efficiency of Double Halide Perovskites M_2KIrCl_6 (M = Cs, Rb) through DFT and SCAPS-1D, *Langmuir*, 2025, **41**(30), 19797–19820.
56 A. V. Kosobutsky, *et al.*, First principles study of electronic structure and optical properties of $LiMTe_2$ (M = Al, Ga, In) crystals, *J. Phys. Chem. Solids*, 2010, **71**(5), 854–861.
57 M. Jamil, *et al.*, Investigations of the structural, mechanical and optoelectronic attributes of $Rb_2TlB'I_6$ (B′ = As, Ga) double perovskites for photovoltaics, *J. Inorg. Organomet. Polym. Mater.*, 2024, **34**(9), 3984–3994.
58 M. U. Din, *et al.*, Structural, elastic, electronic, optical and thermoelectric response of lead-free double perovskite Rb_2TlInX_6 (X = Cl, I) for energy storage devices: DFT+ SOC investigations, *Mater. Sci. Semicond. Process.*, 2024, **152**, 107081.
59 S. M. H. Qaid, *et al.*, First-principles investigations on the structural, optoelectronic, mechanical and transport properties of new stable lead-free double perovskites $Cs_2BB'I_6$ (B = Ag/Rb, B′ = Bi/Ga) halides, *Mater. Sci. Eng., B*, 2024, **301**, 117176.
60 *Handbook of Semiconductors: Fundamentals to Emerging Applications*, ed. R. K. Gupta, *et al.*, CRC Press, 2024.
61 T. Nakajima, *et al.*, Discovery of Pb-Free Perovskite Solar Cells *via* High-Throughput Simulation on the K Computer, *J. Phys. Chem. Lett.*, 2017, **8**(19), 4826–4831.
62 S. Mahmud, *et al.*, DFT aided prediction of phase stability, optoelectronic and thermoelectric properties of A_2AuScX_6 (A = Cs, Rb; X = Cl, Br, I) double perovskites for energy harvesting technology, *Vacuum*, 2024, **221**, 112926.
63 M. T. Jamil, *et al.*, Effect on structural and optical properties of Zn-substituted cobalt ferrite $CoFe_2O_4$, *J. Ovonic Res.*, 2017, **13**(1), 45–53.
64 M. Nait Amar, *et al.*, Prediction of Lattice Constant of A_2XY_6 Cubic Crystals Using Gene Expression Programming, *J. Phys. Chem. B*, 2020, **124**(28), 6037–6045.
65 M. Tarekuzzaman, *et al.*, Caesium-Based Perovskite Hydrides: A Theoretical Insight into Hydrogen Storage and Optoelectronic Characteristics, *Solid State Commun.*, 2025, **404**(1), 116043.
66 M. Wuttig, *et al.*, Halide Perovskites: Advanced Photovoltaic Materials Empowered by a Unique Bonding Mechanism, *Adv. Funct. Mater.*, 2022, **32**(2), 2110166.
67 T. Saha, *et al.*, Thermodynamic and dynamic stability in a new potential $Cs_2AgAsCl_6$ perovskite: insight from DFT study, *Phys. Chem. Chem. Phys.*, 2022, **24**(43), 26609–26621.
68 M. U. Din, *et al.*, Scrutinized the spin-orbit coupling effect on the elastically and thermodynamically stable Rb_2BCl_6 (B = Pb, Ti) double perovskites for photocatalytic, optoelectronic and renewable energy applications, *Mater. Sci. Semicond. Process.*, 2023, **163**, 107569.
69 H. Ehrenreich, *et al.*, Self-Consistent Field Approach to the Many-Electron Problem, *Phys. Rev.*, 1959, **115**(4), 786–790.
70 M. Caid, *et al.*, Comprehensive exploration of halide double perovskites $Cs_2B'GeCl_6$ (B′: Zn, Cd) for affordable energy technologies: a high-throughput investigation, *Opt. Quantum Electron.*, 2024, **56**(6), 980.
71 M. S. Parves, *et al.*, Optimized Solar Conversion Achieved with Double Halide $X_2NaIrCl_6$ (X = Rb, Cs) Perovskites for Optoelectronic and Photovoltaic Applications, *Energy Nexus*, 2025, **20**, 100549.
72 M. S. Parves, *et al.*, Structural and optoelectronic study of $MgLiX_3$ (X= Cl, Br, and I) halide perovskites: A DFT approach, *AIP Adv.*, 2024, **14**, 10.
73 Z.-J. Liu, *et al.*, Structural, Electronic and Optical Properties of the Tetragonal Phase of $CaSiO_3$ Perovskite under Pressure: First-Principles Calculations, *Mod. Phys. Lett. B*, 2011, **25**(01), 41–52.
74 A. El Amrani, *et al.*, Determination of the suitable refractive index of solar cells silicon nitride, *Superlattices Microstruct.*, 2014, **73**(1), 224–231.
75 J. Xie, *et al.*, Perovskite Solar Cells Processed by Solution Nanotechnology, *Advanced Nanomaterials for Solar Cells and Light Emitting Diodes*, 2019, pp. 119–174.
76 V. Antonov, *et al.*, *Electronic structure and magneto-optical properties of solids*, Springer Science & Business Media, 2006.
77 Y. Liu, *et al.*, Hexagonal Lead-Free Cs_2AgBiI_6 Perovskite Nanocrystals: A Promising Material for Solar Cell Application, *ACS Appl. Energy Mater.*, 2023, **6**(10), 5188–5196.
78 T.-Y. Tang, *et al.*, An ab-initio investigation of novel double halide perovskite Cs_2InCoX_6(X = F, Cl, Br) materials with direct band structure and broadband light absorption, *Mater. Sci. Semicond. Process*, 2022, **152**(1), 107047.
79 D.-Y. Hu, *et al.*, First-principles study on the structural, elastic, electronic and optical properties of lead-free double perovskites Cs_2CuBiX_6 (X = I, Br, Cl), *Mater. Today Commun.*, 2021, **29**, 102842.
80 M. U. Din, *et al.*, Electronic structure and optical response of double perovskite Rb_2NaCoF_6 for optoelectronic devices, *Phys. B*, 2022, **627**, 413533.
81 M. Irfan, *et al.*, New eco-friendly lead-free double perovskites Rb_2FeCdO_6 driven semiconducting material for radiation shielding and energy applications: DFT + U based nano architectonics, *Opt. Quantum Electron.*, 2024, **56**(8), 1355.
82 A. B. Siad, *et al.*, Elevating energy device potential: exploring optoelectronic and thermoelectric advantages in stable double perovskites K_2NaInX_6 (X = F, Cl, Br, I) *via* Ab initio analysis, *J. Mater. Sci.*, 2024, **59**(5), 1989–2007.
83 S. Al-Qaisi, *et al.*, A comprehensive first-principles computational study on the physical properties of lutetium aluminium perovskite $LuAlO_3$, *Mater. Chem. Phys.*, 2020, **250**(1), 123148.
84 E. Haque, *et al.*, First-principles study of elastic, electronic, thermodynamic, and thermoelectric transport properties of TaCoSn, *Results Phys.*, 2018, **10**(1), 458–465.

85 G. K. H. Madsen, *et al.*, BoltzTraP. A code for calculating band-structure dependent quantities, *Comput. Phys. Commun.*, 2006, **175**(1), 67–71.
86 G. A. Slack, *et al.*, Nonmetallic crystals with high thermal conductivity, *J. Phys. Chem. Solids*, 1973, **34**(2), 321–335.
87 S. Mahmud, *et al.*, Investigation of direct small bandgap Cs_2AuInX_6 (X = F/Cl) double perovskites for energy harvesting technology employing DFT, *Comput. Condens. Matter*, 2024, **40**, e00950.
88 S. Mahmud, *et al.*, Prediction of X_2AuYZ_6 (X = Cs, Rb; Z = Cl, Br, I) double halide perovskites for photovoltaic and wasted heat management device applications, *J. Phys. Chem. Solids*, 2025, **169**, 112298.
89 Q. Mahmood, *et al.*, Role of 5d orbital of Re in ferromagnetism and thermoelectric characteristics of Cs_2ReCl/Br_6 double-perovskites: a density functional theory study, *Eur. Phys. J. Plus*, 2020, **135**(9), 1–13.
90 S. Niaz, *et al.*, Bandgap tuning and thermoelectric characteristics of Sc-based double halide perovskites K_2ScAgZ_6 (Z = Cl, Br, I) for solar cell applications, *J. Phys. Chem. Solids*, 2023, **174**(1), 111115.
91 T. Wu, *et al.*, Development of perovskite-type materials for thermoelectric application, *Materials*, 2018, **11**(6), 999.
92 S. Berri, *et al.*, Density functional theory calculations of electronic structure and thermoelectric properties of K-based double perovskite materials, *Energy Storage*, 2023, **5**(1), e400.
93 E. Schreiber, *et al.*, Elastic Constants and Their Measurement, *J. Appl. Mech.*, 1975, **42**(3), 747–748.
94 B. Ghebouli, *et al.*, An ab initio study of the structural, elastic, electronic, optical properties and phonons of the double perovskite oxides Sr_2AlXO_6 (X = Ta, Nb, V), *Mater. Sci. Semicond. Process.*, 2016, **42**, 405–412.
95 Z. Sun, *et al.*, Theoretical investigation of the bonding and elastic properties of nanolayered ternary nitrides, *Phys. Rev. B:Condens. Matter Mater. Phys.*, 2005, **71**(19), 193402.
96 J. C. Wei, *et al.*, Theoretical investigation of the elastic, Vickers hardness and thermodynamic properties of δ-WN under pressure, *Mater. Sci. Semicond. Process.*, 2014, **27**, 883–890.
97 H. Belhadj, *et al.*, Optical properties of $(Pb_{1-x}Mn_xS)_{1-y}Fe_y$ materials from first-principles calculations, *Chin. J. Phys.*, 2017, **55**(3), 1032–1043.
98 A. Siddique, *et al.*, Structural, electronic, mechanical and dynamical stability properties of $LiAH_3$ (A = Sc, Ti & V) perovskite-type hydrides: a first principle study, *Chem. Phys.*, 2023, **568**(1), 111851.